JPhys Materials

TOPICAL REVIEW • OPEN ACCESS

MXene-based 3D porous macrostructures for electrochemical energy storage

JPhys Materials

OPEN ACCESS

RECEIVED
29 November 2019

REVISED
17 January 2020

ACCEPTED FOR PUBLICATION
21 February 2020

PUBLISHED
7 April 2020

TOPICAL REVIEW

MXene-based 3D porous macrostructures for electrochemical energy storage

G Tontini, M Greaves, S Ghosh, V Bayram and S Barg

Department of Materials, Faculty of Science and Engineering, The University of Manchester, Manchester, United Kingdom

E-mail: suelen.barg@manchester.ac.uk

Keywords: MXenes, 3D architectures, 2D metal carbides, energy storage, batteries, supercapacitors, 2d materials

Abstract

2D transition metal carbides and nitrides (MXenes) have shown outstanding potential as electrode materials for energy storage applications due to a combination of metallic conductivity, wide interlayer spacing, and redox-active, metal oxide-like surfaces capable of exhibiting pseudocapacitive behavior. It is well known that 2D materials have a strong tendency to restack and aggregate, due to their strong van der Waals interactions, reducing their surface availability and inhibiting electrochemical performance. In order to overcome these problems, work has been done to assemble 2D materials into 3D porous macrostructures. Structuring 2D materials in 3D can prevent agglomeration, increase specific surface area and improve ion diffusion, whilst also adding chemical and mechanical stability. Although still in its infancy, a number of papers already show the potential of 3D MXene architectures for energy storage, but the impact of the processing parameters on the microstructure of the materials, and the influence this has on electrochemical properties is still yet to be fully quantified. In some situations the reproducibility of works is hindered by an oversight of parameters which can, directly or indirectly, influence the final architecture and its properties. This review compiles publications from 2011 up to 2020 about the research developments in 3D porous macrostructures using MXenes as building blocks, and assesses their application as battery and supercapacitor electrodes. Recommendations are also made for future works to achieve a better understanding and progress in the field.

1. Introduction

Since the popularisation of two-dimensional (2D) materials with the isolation of graphene in 2004 [1], one of the biggest challenges for their practical application as bulk materials is their tendency to agglomerate and re-stack [2]. To circumvent this problem, techniques to engineer these materials into three-dimensional (3D) architectures while retaining their unique 2D properties are continually investigated.

A wide range of techniques, such as template assisted methods, self-assembly methods and 3D printing techniques have been employed to build 3D structures from graphene or reduced graphene oxide (rGO) with applicability in areas such as energy conversion, energy storage, catalysis, environmental cleaning, and biological applications [2–5]. Beyond graphene, other nanomaterials such as hexagonal boron nitrides [6], and metal oxides and hydroxides [7] were later developed and studied, and showed similar challenges for their application as bulk materials, cultivating more interest in techniques to use 2D materials as building blocks for 3D architectures.

In 2011, Naguib *et al* [8] reported, for the first time, the production of 2D $Ti_3C_2T_x$ nanocrystals by selective etching of Ti_3AlC_2 giving origin to an entirely new family of 2D materials composed of transition metal carbides, nitrides, and carbonitrides, called MXenes, with promising potential for energy storage applications [9]. Currently known MXenes present the general formula $M_{n+1}X_nT_x$ ($n = 1, 2$ or 3), or more recently also $M_{1.33}XT_x$, where M represents an early transition metal (such as Sc, Ti, Zr, Hf, V, Nb, Ta, Cr, and Mo), X is

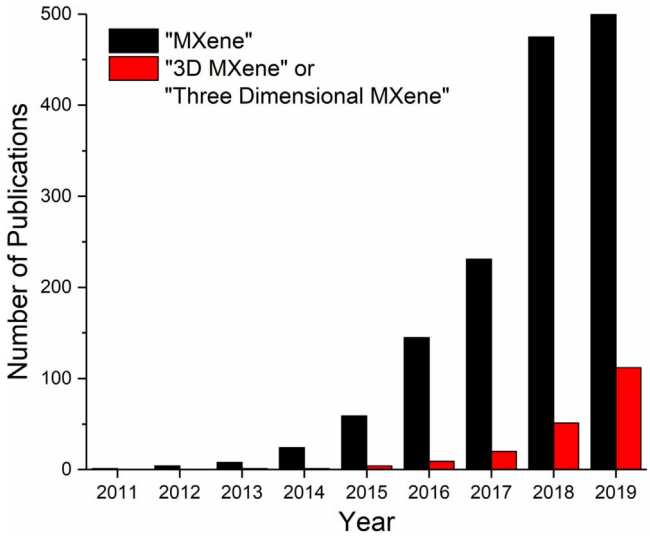

Figure 1. Number of scientific articles with the keywords 'MXene' (black bars) and '3D MXene'/'Three Dimensional MXene' (red bars) over the past few years up to 2019 (source: www.webofknowledge.com).

carbon and/or nitrogen and T_x represents surface terminations which vary depending on the synthesis method used (for example, hydroxyl, oxygen, or fluorine) [10].

With less than 10 years since their discovery, efforts are still mainly pointed towards the assessment of its potentialities and exploration of its properties, while their integration and application in various engineering fields are still very much in their infancy. Nevertheless, investigations have shown very competitive results in energy storage devices attracting a lot of interest in the field. In particular, the inner conductive metal carbide layers provide fast electron supply to electrochemically active sites, and functional groups on the surface, allow water intercalation and fast redox activity for pseudocapacitive energy storage [11–13]. Besides energy storage, MXenes also showed promising properties and have been researched for a variety of other areas, such as electromagnetic shielding, environmental, sensors, optoeletronic devices, and renewable energy [9, 14–16].

For most practical applications, the MXene powders must be assembled or processed into a macroscopic sample such as, for example, an electrode. Conventionally this is done either by mixing it with a solvent to form a slurry which is painted over a substrate, by directly vacuum filtration, by spin coating, or by spraying the MXene suspension to form a compact film. During these processes, there is limited control over the 2D flakes assembly and a stacked structure is normally formed, hindering their surface-dependent properties. For example, supercapacitor film electrodes made by rolling MXene-clay [17], whilst showing good volumetric capacitance values, achieve comparatively low gravimetric capacitance (900 F cm^{-3} and 245 F g^{-1} at 2 mV s^{-1} in H_2SO_4) and low rate capability due to poor ion transport within the stacked structure. Several intercalation and hybridization strategies have been applied to prevent this restacking as reviewed by Liu *et al* [18].

Reviews on 3D ordered porous [19], heterogeneous nanostructured [20] and multidimensional materials [21] emphasize the importance of ionic accessibility to the redox-active sites, discussing the impact of both micro- and macro-scale structures on electrochemical energy storage performance. On the crystallographic level, for example, a work with different MnO_2 allotropic phases by Ghodbane *et al* [22] and reviewed by Lukatskaya *et al* [21], shows that an increase in channel size and connectivity resulted in improved electrochemical performance. Further designing hierarchical, 3D macrostructures, as exhaustively shown for graphene-based materials, can further overcome some of the restacking limitations of 2D materials, providing light weight structures with high porosity, large specific surface area, high electrical conductivity and stable chemical and mechanical properties [2, 5]. However, there is a trade-off to be made, as excessive porosity leads to lower active material density, reducing the volumetric capacitance of the materials [23].

As shown in figure 1, research into the MXene' family grew exponentially over the past few years, with several excellent review articles of synthesis methods and properties [10, 11, 24–26] summarizing its fast advancement. Nevertheless, the exploration of 3D assemblies using MXenes as building blocks still lacks research, having about 200 scientific papers published since its first report up to 2020, mostly using various forms of $Ti_3C_2T_x$, and there is no progress report to gather, expose and discuss the results of the applied processing techniques. Thus, this review article focuses on presenting the current progress in the application of known processing techniques to form 3D porous structures using MXenes as building blocks, critically analyses the achieved microstructures and discuss the results obtained by such materials as battery and supercapacitor electrodes.

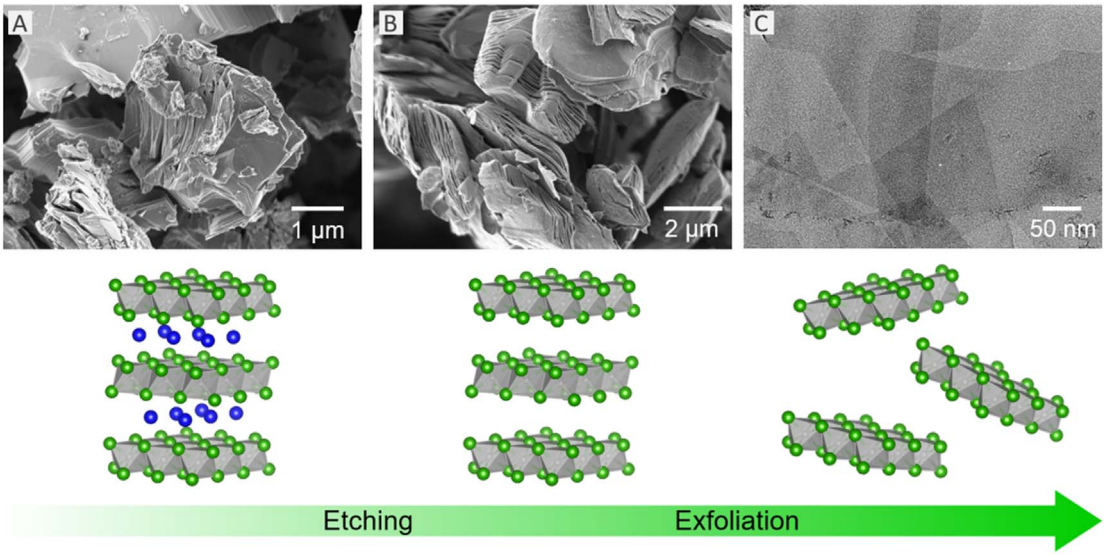

Figure 2. Pathway to obtain 2D MXene single flakes by typical top-down synthesis: First, selective etching of atomic layer(s) from a 3D layered precursor is required, and then exfoliation into single flakes. (A) SEM micrograph of Ti_3AlC_2 particles. (B) SEM micrograph of $Ti_3C_2T_x$ multilayers after etching of the Al layer. (C): TEM micrograph of overlapping $Ti_3C_2T_z$ single layers. Schematics of the MAX to multilayers MXene transformation and their exfoliation are shown in bottom row [10]. Reprinted from [10], Copyright (2019), with permission from Elsevier.

2. Preparation of MXene

MXenes are often made via a top-down approach by selective etching of certain atomic layers from their layered precursors, such as MAX phase, which are made of layers of transition metal carbides or nitrides ($M_{n+1}X_n$) interleaved by layers of A-element atoms (mostly group 13 and 14 of the periodic table). The M–A bonds are more chemically reactive than the stronger M–X, allowing the selective etching of the A-element layers [10]. For example, when an Al-based layered carbide MAX powder (such as Ti_3AlC_2) is placed into a solution of hydrofluoric acid (HF) or an acidic aqueous solution that can provide in situ formation of HF (for example, HCl + LiF), the A-element layer is selectively etched and replaced with hydroxyl, oxygen and fluorine surface terminations (T_x), forming multilayered MXenes [24]. It has been shown that the resulting T_x composition and distribution is strongly dependent on synthesis method [10, 27, 28], and will directly influence the MXene's properties, relevant to processing and applications. For example, a nuclear magnetic resonance (NMR) spectroscopic study showed that $Ti_3C_2T_x$ produced by *in situ* formation of HF (from HCl and LiF reaction) contains considerably fewer fluorine terminations than that synthesized with HF solution directly [28]. Recently, alternative synthesis routes were able to produce fluorine-free terminations [29–35] and even fully chlorinated MXenes [34].

Intercalation of a number of substances, such as water, cations, dimethyl sulfoxide (DMSO), tetrabutylammonium hydroxides (TBAOH) or surfactants into the interlayer spacing, followed by sonication makes it possible to exfoliate MXenes to produce single-flake suspensions and prevent them from restacking [11, 18, 24, 36]. Minimally Intensive Layer Delamination (MILD), currently the most popular synthesis method, is able to produce large MXene flakes with fewer defects, in which the resulting intercalated layers can be easily delaminated with no sonication needed [24]. Figure 2 presents a simplified pathway to obtain 2D MXene single flakes from etching to exfoliation and micrographs of the material on the respective stages of the process.

About 30 different MXene phases have been successfully synthesized since its conception, mostly layered carbides via selective etching by aqueous fluoride-containing acid solutions (HF, HCl/LiF, NH_4HF_2) [10]. The few nitride MXenes reported were obtained using a molten eutectic fluoride salt mixture of LiF, NaF and KF at high temperatures [37] or by ammoniation of previously obtained carbide MXenes [38]. Fluorine-free syntheses are still arguably still barely explored by the literature, with only a few methods reported such as electrochemical etching [29–31], hydrothermal alkali treatment [32, 33, 35] and reaction with Lewis acidic molten salt [34]. For a more complete overview of the different synthesis' routes toward MXenes and other ultrathin 2D transition metal carbides and nitrides to date, the reader can refer to Verger *et al* works [10, 39].

3. Revision methodology

A systematic literature search was conducted to identify papers published between January 2011 and January 2020. Firstly, recurrent computer searches were performed on Google Scholar and Web of Science databases utilizing the search terms: '3D MXene' or 'Three dimensional MXene' or '3D Ti_3C_2' or 'Three dimensional Ti_3C_2'. Studies were then excluded for any of the following reasons: (I) Single or multilayered MXene were not present in the final architecture (e.g.: studies with MXene-derived carbon); and (II) MXene stacking was not total or partially prevented in any way, forming layer-over-layer thin films with no distinct microstructure (e.g.: vacuum filtering of delaminated MXene). Secondly, sources cited in relevant literature obtained from the first step were manually checked and added, as well as associated references when appropriate. As studies with MXene phases different from $Ti_3C_2T_x$, such as Ti_2CT_x, Mo_2CT_x and V_2CT_x are still very scarce, 3D assemblies of these compositions were further manually searched and reviewed following the same conditions. 3D architectures on which MXenes are not the main phase of the supporting structure, but only coated or attached to a different material scaffold (such as graphene aerogels, polymer framework and Ni-Foam), were also reviewed and referenced, but not discussed in detail as it deviates from the original goal of the review. After discussing the processing techniques and morphologies obtained, the works focused on electrochemical energy storage were further analyzed and critically discussed regarding the role of MXene 3D porous architectures, how they have been employed and significant concerns or challenges identified. The data presented in this review were extracted from text, tables and plots of the referenced works and their respective supplementary data, prioritizing extracted plot data in case of large discrepancies. Plot data was extracted using the open source software WebPlotDigitizer (Version 3.9) available at http://arohatgi.info/WebPlotDigitizer.

4. MXenes 3D assembly techniques

The construction of 3D structures with 2D materials using colloidal-based approaches mainly involves self- and directed assembly (which normally relates to the flake-flake interactions and interfacial assembly) or template-assisted methods (e.g. the use of a sacrificial phase to control the porosity and organization of the 2D material within the pores at a larger scale). Very often the processing route will involve a combination of both methods in order to enable the formation of stable films or macrostructures with controlled microstructure and porosity.

We categorise the review into the development of processing routes to assemble: (I) MXene '3D nanostructured particles'; (II) MXene '3D porous films' and (III) MXene '3D porous macrostructures'. This allows the reader to see the evolution of structural control from the nano- and micrometre scale (e.g.: crumpled particles and hollow spheres) up to macrostructures of more practical dimensions (e.g.: 3D printed architectures). In particular, the hydrophilicity of MXenes (rendered by their surface functional groups, such as –O, –OH and –F) allows them to be easily dispersed in aqueous suspensions and inks playing a great advantage for their processing using the different approaches reviewed in I–III.

4.1. MXene 3D nanostructured particles

MXenes, like other 2D materials, have a strong tendency to agglomerate and re-stack, reducing their specific surface area, and hence losing their desirable properties. The assembly of 2D flakes into nanostructured three-dimensional particles is a valid approach to overcome stacking [40–45].

Following this strategy, 2D $Ti_3C_2T_x$ flakes were assembled on the surface of sacrificial poly(methyl methacrylate) (PMMA) spheres to produce hollow spheres (figure 3(A)) [13, 40]. This method allows the tuning of size and thickness of the hollow MXene spheres by changing the sacrificial template size (ca. 200 nm–2 μm) and mass ratio in relation to MXene.

By spray drying a highly dilute (0.1 mg ml^{-1}) aqueous dispersion of $Ti_3C_2T_x$ nanosheets (ζ-potential ca.—34 mV), Shah *et al* showed that the flakes encapsulated within spray-dried droplets can be scrolled, bent, and folded into crumpled structures due to the capillary forces on the evaporating droplets (at 220 °C) [41]. They have reported that higher concentration of MXene leads to less crumpling due to the stacking of the flakes inside the droplets, raising their stiffness. Upon rehydration, such morphological changes were found to be almost completely reversible. Despite this work's effectiveness in manipulating the morphology, during the spray drying process (at 220 °C), according to XPS analysis, the titanium oxidizes up to about 25 wt%. Later, Xiu *et al* applied similar process to produce 3D crumpled structures of MXene (figure 3(B)) through ultrasonic nebulization, but under a considerably higher temperature of 600 °C, under Argon atmosphere to prevent oxidation [45]. They show a dependence on the initial concentration of MXene colloids, but did not observe reversibility upon rehydration like Shah *et al*, possibly due to the larger thermal and capillary forces of this approach that can introduce defects into the flakes. Aside from spray drying, crumpled morphologies were also shown to be obtainable by dispersing MXenes in strong acids and alkalis [42–44].

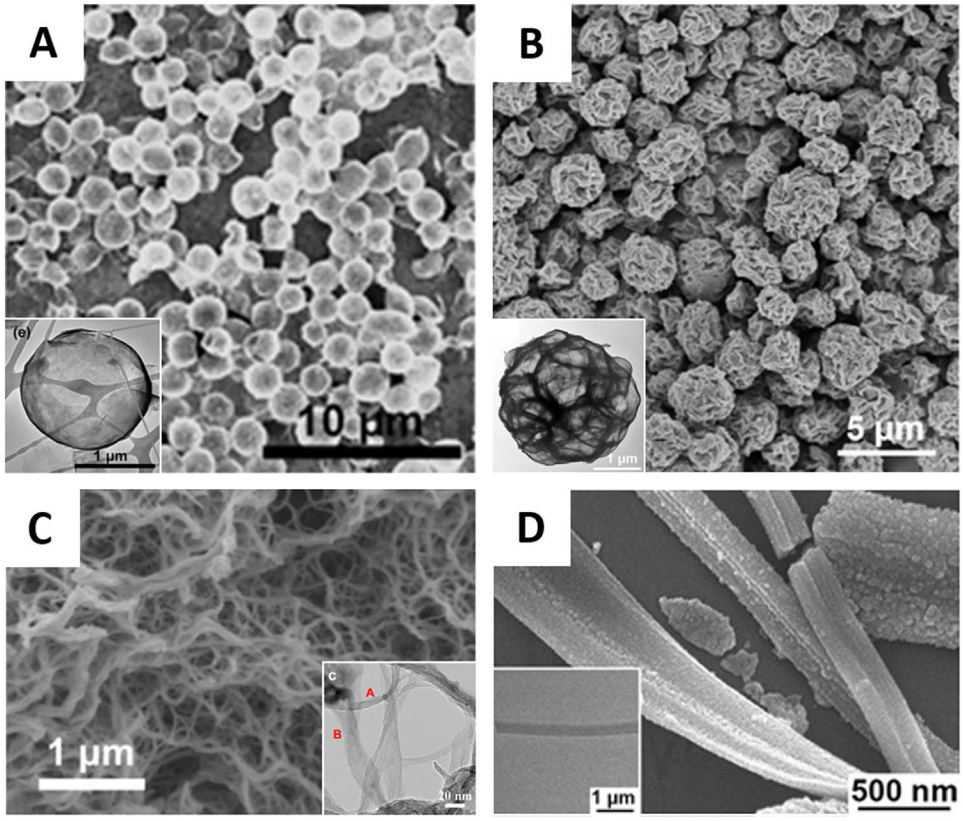

Figure 3. SEM and TEM (insets) images of different self-assembled $Ti_3C_2T_x$ 3D particles morphologies. (A) Hollow-spheres [40]. [40] John Wiley & Sons. (B) Crumpled particles [45]. Reprinted with permission from [45]. Copyright © 2018 American Chemical Society. (C) Narrow alkalized nanoribbons [46]. Reprinted from [46], Copyright (2017), with permission from Elsevier. (D) Fluorine-free wide nanoribbons [35]. Reprinted from [35], Copyright (2019), with permission from Elsevier.

There are also studies and reports of MXene narrow nanoribbons networks (figure 3(C)) for use in high-performance sodium and potassium batteries [46] and lithium–sulfur batteries [47]. Lian *et al*, for example, reported the fabrication of 3D porous frameworks of alkalized $Ti_3C_2T_x$ (a-$Ti_3C_2T_x$) nanoribbons by continuous shaking HF-etched MXene in aqueous KOH solution for 72 h, during which alkalization occurs simultaneously with exfoliation [46]. A wide nanoribbon morphology (~700 nm) was also recently obtained by a fluorine-free hydrothermal method at 180 °C in KOH solution as shown in figure 3(D) [35].

Besides morphology manipulation, hybridization of the MXene flakes can also generate 3D particle structures with enhanced and tunable properties. Due to their surface functional groups, MXene flakes can be used as substrate to grow structures such as MoS_2, amorphous carbon or layered double hydroxides [48–50]. Wu *et al*, for example, produced hierarchical carbon coated $Ti_3C_2T_x/MoS_2$ nanohybrids via an *in situ* and simultaneous hydrothermal synthesis of MoS_2 and amorphous carbon nanoplating over MXene flakes that not only prevents stacking and improve electrochemical properties, but also considerably improves their oxidation resistance [48].

4.2. MXene 3D porous films

Upon developing and manipulating the 3D morphology of particles as described in the previous section, they can be further used as 'building blocks' to form porous films with complex microstructures suitable for energy and other applications. For example, *via* simple vacuum filtration of these materials, a film with micro-, meso-, or macroporosity (or, most likely, a combination of these) can be achieved with lower densities and larger specific surface area than a more compact equivalent [42–47, 49, 50]. Figure 4 shows porous films obtained by different approaches. Figure 4(A), for example, shows an alveolar porosity (~1 to 2 μm in diameter) formed *via* vacuum filtration of the aforementioned MXene hollow spheres, achieving a flexible film with a density of *ca.* 0.4 g cm^{-3} (figure 4(B)). The structure also roughens the film's surface, leading to hydrophobicity with a large contact angle of 135° [40]. Similarly, a porous crumpled film, with average pore sizes smaller than 1 μm, can be formed by vacuum filtering pre-made MXene crumpled particles as shown in figure 4(C) [45].

Another approach to generate a 3D foam-like material was reported by Liu *et al* [51]. By treating a vacuum filtered compact film (figure 4(D)) of $Ti_3C_2T_x$ impregnated with hydrazine at 90 °C it is expanded (or inflated),

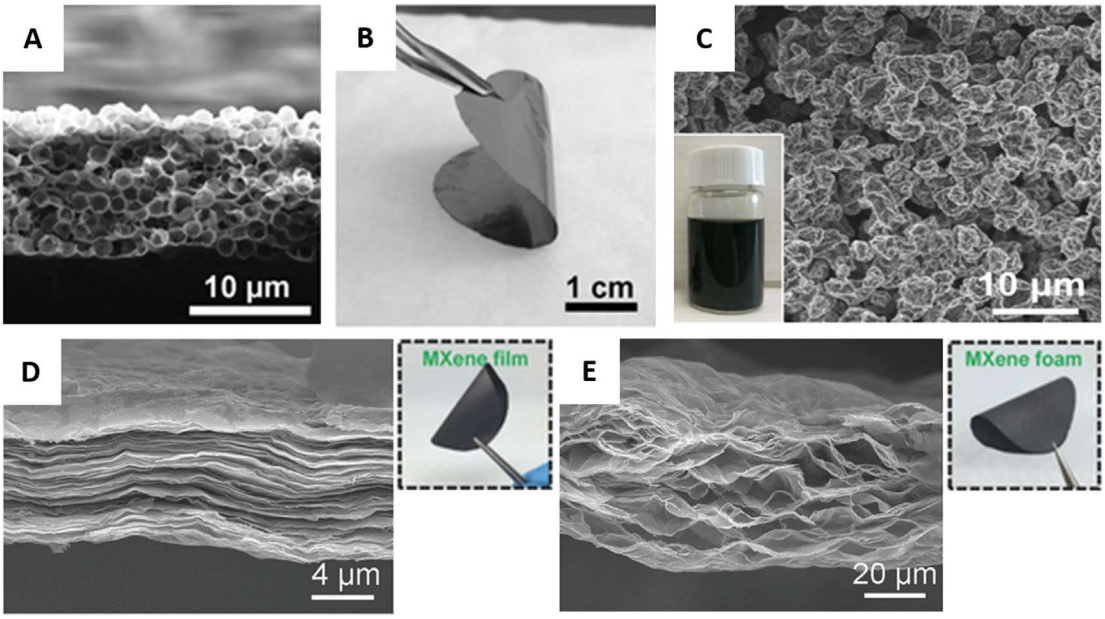

Figure 4. (A) Cross-sectional SEM image of 3D macroporous film formed by $Ti_3C_2T_x$ hollow-spheres and (B) digital image showing the flexibility of the respective macroporous film [40]. [40] John Wiley & Sons. [© 2017 WILEY-VCH Verlag GmbH & Co. KGaA, Weinheim]. (C) SEM image of macroporous film of crumpled $Ti_3C_2T_x$ after compression test under 150 MPa (inset: film pre-cursor aqueous suspension) [45]. Reprinted with permission from [45]. Copyright (2018) American Chemical Society. (D) Cross-sectional SEM image and digital image of vacuum filtered $Ti_3C_2T_x$ film and (E) and its respective expanded foam via hydrazine treatment [51]. [51] John Wiley & Sons. [© 2017 WILEY-VCH Verlag GmbH & Co. KGaA, Weinheim].

creating a porous structure with pore sizes on the order of 10 μm (figure 4(E)). It is proposed that the hydrazine reacts with the MXene termination groups, rapidly releasing gaseous species and generating enough pressure to overcome van der Waals forces between sheets. It is also verified that the porous structure can be tuned by varying the dosage of hydrazine. By a similar route, Ma *et al* produced Ti_3C_2/rGO hybrid foams by subjecting Ti_3C_2/GO films to hydrazine vapor at 90 °C for 10 h and a further annealing step [52].

Bao *et al* reported the production of porous films by freezing a $Ti_3C_2T_x$ suspension in liquid nitrogen and subsequently freeze-drying it [53]. The obtained aerogel-like powder underwent conventional electrode fabrication by mixing with carbon black and a solvent (Nmethyl-2-pyrrolidone, NMP) to make a slurry that can be pasted onto a substrate to form a porous MXene-based architecture. Although SEM images of the freeze-dried powder show particles with a clear porous structure, no microstructural characterization of the final electrode was provided to assess if and how the slurry processing affected the morphology of the pores.

Although still broadly considered thin films, the control of size and shape of the pores within these porous films may lead to different properties than their stacked 2D layers counterparts, arguably introducing the same dimension of complexity as larger 3D architectures.

4.3. MXene 3D porous macrostructures

Here we review the methods that allow the fabrication of porous macrostructures where the internal microstructure extends throughout the three-dimensions with practical sizes and shape control that goes beyond the capabilities of the film fabrication approaches described in the previous session. Both the macrostructure design (i.e. the shape) and microstructure (i.e. pore size, morphology, and distribution) of the fabricated sample are dependent on the fabrication method and may be tuned by its processing parameters. A variety of techniques for assembling 2D MXenes into 3D porous macrostructures have been reviewed and were divided into the following sections: (I) assembly by induced gelation; (II) freeze-casting; (III) alternative template-assisted techniques; and (IV) additive manufacturing.

4.3.1. Assembly by induced gelation

One of the first concerns with the assembly of MXene architectures is their weak gelation capability (see GO) [54], which reduces the connections between sheets and hinders their mechanical stability. Therefore, if the concentration is too low, for example, a freeze-dried MXene colloid collapses into a powder of aerogel-like porous particles [53]. To overcome this problem, additives such as ethylenediamine (EDA) [55], thiourea dioxide (thiox) and ammonia [56], PAA [57], and divalent metal ions [54], have been used to functionalize the $Ti_3C_2T_x$ sheets and enhance their interconnectivity during the gelation process [54–57]. The mechanism that

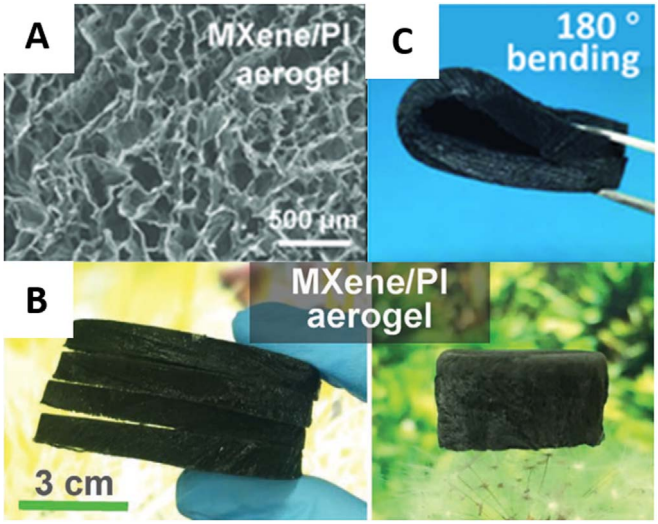

Figure 5. (a) SEM image revealing the porous structure; (b) digital images of MXene/PI aerogels; (c) and representation of their excellent flexibility [57]. [57] John Wiley & Sons. [© 2018 WILEY-VCH Verlag GmbH & Co. KGaA, Weinheim].

induces gelation depends on the additive used and can be via a chemical reduction of the surface of the sheets (when using mild reducing agents, such as EDA, thiox and ammonia, or PAA), or simple electrostatic interactions of the surface functional groups and the cross-linking agent (e.g. in the case of divalent metallic ions).

Through the functionalization of the MXene flakes with ethylenediamine (EDA), Li *et al* assembled 2D MXenes into a 3D network (or '3D aerogel') with a specific surface area of 176.3 $m^2\ g^{-1}$ measured with Brunauer–Emmett–Teller (BET) method [55]. Although some samples were shown to have a radially oriented porosity, attributed to the shape of the vial where the suspension was frozen, freezing parameters were provided without sufficient detail (such as cooling rate and freezing direction) to enable reproduce the result. Nevertheless, a similar structure was obtained by Wang *et al* via bidirectional freeze-casting, and more deeply investigated for GO aerogels [58].

Other functionalization strategies to improve gelation and mechanical resistance were also reported [54, 56, 57]. Wang *et al* produced a $Ti_3C_2T_x$ aerogel using thiox and ammonia solution to prevent oxidation of the sheets after hydrolysis and to enhance the formation of interconnected nanosheets [56]. The free-standing aerogel obtained by this route presented a density of ~27 mg cm^{-3} and XPS analysis showed N–O and N–Ti bonds indicating N incorporation into the $Ti_3C_2T_x$. Alternatively, polyamic acid (PAA) can be mixed with a MXene suspension prior to the freeze-drying process [57]. Further thermal annealing of this MXene/PAA aerogels at 300 °C under an argon atmosphere induces PAA polymerization into polyimide (PI) macromolecular bridges and forming a MXene/PI composite (figure 5(A)), which not only link the MXene sheets but also give the composite superelastic properties (figure 5(B)) such as 80% reversible compressibility, excellent fatigue resistance, and 20% reversible stretchability.

Divalent metal ions, such as Fe^{2+}, Ni^{2+} and Co^{2+}, can also improve the gelation of MXene by bonding with the –OH terminations (cation-induced gelation), hindering the electrostactic repulsive forces and, acting as joining sites [54]. Trivalent metal ions such as Al^{3+} can also initiate gelation, but most of them, such as Fe^{3+} and Co^{3+}, are shown to oxidize the MXenes [54]. The use of univalent ion K^+ has lead to the coagulation of MXene without forming a stable hydrogel [54]. Depending on the ion type, and its ratio to MXene used for the gelation process, freeze-dried monoliths of the respective hydrogels present significantly different microstructures, with varying pore size in the micrometre range (figure 6). The freeze-dried monoliths of MXene gelated with Fe^{2+} have a specific surface area of 27 $m^2\ g^{-1}$ as measured by nitrogen absorption isotherms using the BET method, which is significantly smaller than reported for MXene-based works with similar morphologies (such as in [53, 55]).

Some works report the formation of hybrid graphene/MXene composites [59–63]. GO can help to stabilize the MXene flakes in the suspension forming a composite sol or gel, making it possible to freeze-dry it. After freeze-drying and further reduction treatment, the reduced graphene oxide (rGO) acts as a scaffold to support MXene sheets providing improved mechanical resistance to the composite. Yue *et al*, for example, fabricated an aerogel micro-supercapacitor of $Ti_3C_2T_x$/rGO composite by this method, and further made it self-healable by incorporating it with a polyurethane matrix [60].

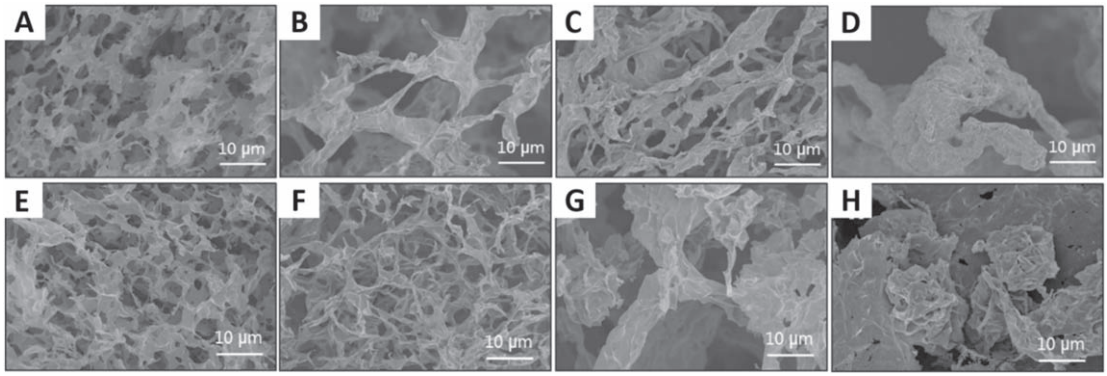

Figure 6. SEM images showing the microstructure of freeze-dried MXene hydrogels made with different metal chloride solutions. Hydrogels made with 50 ml of MXene suspension (10 mg ml^{-1}) in 20 0 μl of (A)–(D) $FeCl_2$ (0.74, 1.97, 3.94 and 7.89 M, respectively); (E) $CoCl_2$ (1 M); (F) $NiCl_2$ (1 M); $AlCl_3$ (1 M); and KCl (1 M) [54]. [54] John Wiley & Sons. [© 2019 WILEY-VCH Verlag GmbH & Co. KGaA, Weinheim].

4.3.2. Freeze-casting

Freeze-casting is a template-assisted processing technique used to turn a solution or suspension into a 3D porous structure which retains the geometrical shape of a pre-designed mould through freezing [64, 65]. When employed effectively, not only the outer design but also the inner morphology, including size and shape of the internal pores can be tuned. This method can generate highly anisotropic structures of ceramics, polymers and more recently 2D materials when a temperature gradient is designed via processing conditions and/or colloidal suspension formulations [66, 67].

During freezing, the microscopic internal walls are formed due to the rejection of particles and/or solute by growing crystals. The final shape of the pores is defined by the ice morphology and by the removal process. Freeze-drying is arguably the most effective method to remove crystal templates (particularly when water is used as the solvent), leading to an almost exact replica of them without collapsing the structure. This technique allows the tuning of the final microstructure through changing suspension characteristics and solidification conditions [64]. Despite water being the most common and studied solidifying fluid, freeze-casting can also be performed with other liquids, allowing an even broader control of pore morphology. Freeze casting can be also employed in combination with a gelation step in order to improve the bonding between individual particles or flakes and so improve mechanical properties as covered on section 4.3.1.

Freeze-casting is a complex approach and the underlying principles that govern the microstructure formation during the process are not yet fully understood, with some parameters that influence these principles still being identified (e.g. environmental conditions, liquid phase composition and mould design). Also, as pointed out by Scotti *et al* in a review compiling almost 900 freeze-casting works [64], many studies present to a certain degree, their own, unique set of parameters, which makes it hard to systematically review the processing-structure-properties relationships.

Despite the increasing number of promising papers being published [58, 68–72], to date, freeze-casting of 2D materials still lacks a dedicated review or progress report to compile, compare, critically analyze and identify the specific challenges the technique presents when applied to different 2D materials.

Freeze-casting of $Ti_3C_2T_x$ suspensions without the use of external supports or cross-linking groups has been reported by Bian *et al,* who showed a correlation between the density of formed aerogels and the $Ti_3C_2T_x$ concentration in the colloidal suspension, reaching densities as low as 4 mg cm^{-3} when a 4 mg ml^{-1} suspension was used [71]. Similar to the other methodologies reported on section 4.3.1, these aerogels (figure 7) were produced by immersing the vial containing MXene suspensions into dry ice bath (−78 °C) for 30 min and then freeze-dried. Although presenting promising results for freeze-cast MXene aerogels, simple immersion into a freezing bath gives little control over the cooling process, not taking true advantage of the microstructural control capabilities of freeze-casting.

Directional freeze-casting (normally inducing unidirectional or bidirectional cooling of colloidal suspensions) provides a better control of the freezing condition and enables the fabrication of cellular structures and aerogels of more defined microstructure and properties. In the case of unidirectional freezing, the crystal dendrites tend to nucleate near a freezing substrate (i.e.: cold finger) and grow roughly perpendicularly to it forming pores highly oriented perpendicularly to the freezing substrate, with a narrow size distribution. In

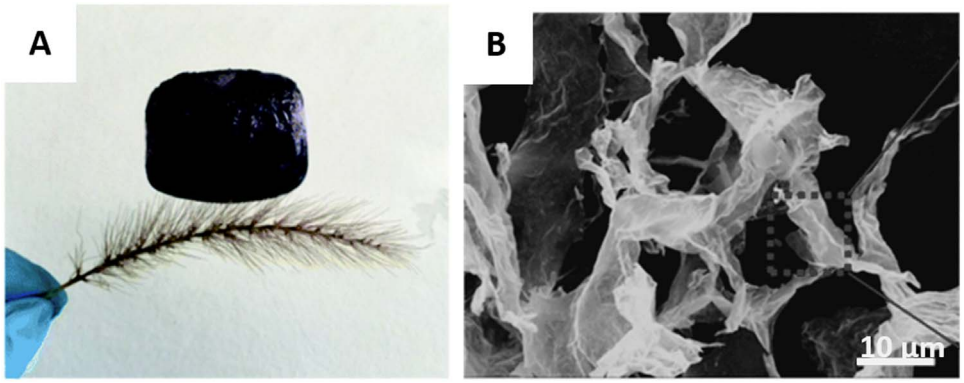

Figure 7. (A) Digital image of freeze-cast $Ti_3C_2T_x$ aerogel (35 cm^3) without crosslinking surface groups standing on a foxtail grass and (B) SEM of its porous microstructure [71]. Reproduced from [71] with permission of The Royal Society of Chemistry.

contrast, bidirectional freeze-casting techniques allow the manipulation of the alignment of the ice crystals simultaneously in two directions [73].

One of the first studies of unidirectional freeze-casting of MXenes was reported by Zhao *et al* to produce a GO-assisted assembled MXene aerogel [61]. Based on the porous architecture, they propose an assembly mechanism as follows: due to their affinity, a stable aqueous $Ti_3C_2T_x$/GO suspension is formed. This suspension is treated with ascorbic acid in autoclave at low temperature (65 °C for 3 h followed by 70 °C for 1 h), which leads to the reduction of the GO forming a hydrogel in which a framework of interconnected rGO sheets is covered by MXene assembled to its surface. The hybrid hydrogel is finally unidirectionally freeze-cast and freeze dried to form a highly oriented architecture with lamellas of ca. 10 μm of width.

A study by Bayram *et al* reported the manufacture of additive-free MXene ($Ti_3C_2T_x$) lamellae architectures by unidirectional freeze-casting for supercapacitor electrodes, and investigated the effect of processing conditions on aerogel architectures and its effect on capacitive performance [72]. Although previous studies showed lamellar architectures formed with the aid of GO, this study aimed to control the morphology only by modifying the freezing parameters, such as concentration and cooling rate. The cooling of MXene suspension (5–50 mg ml^{-1}) at a rate of 5 °C min^{-1} down to −70 °C, and subsequent freeze-drying, created aerogels with tuneable volumetric densities (7–43 mg cm^{-3}), lamellar spacing between 28 and 48 μm, and porosities above 99%. With the increase in suspension concentration, the lamellae walls are denser (with less openings present) and more interconnected by bridges. This work also shows that the aerogels microstructures can be further tuned for energy storage by pressing and rolling (with a calendaring machine). The change in the morphology was additionally analyzed by SEM and X-ray computed tomography (microCT), and the effect of pore architecture on capacitive performance was investigated.

Using a bidirectional freeze-casting technique, Han *et al* reported additive-free, aligned, lamellar and macroporous MXene ($Ti_3C_2T_x$, Ti_2CT_x and Ti_3CNT_x) aerogels for electromagnetic shielding [70]. The bidirectional growth of ice crystals arranges MXene flakes into a long range alignment of the lamellar architecture (figure 8). It was also shown that by increasing the starting concentration of colloidal $Ti_3C_2T_x$ from 6 to 12 mg ml^{-1}, the resulting aerogels become denser (5.5 mg cm^{-3} to 11.0 mg cm^{-3}, respectively) and more interconnected. When the concentration of MXene is low (6 mg ml^{-1}) the resultant lamellar spacing is 100–150 μm and few interconnections are observed, while for higher concentrations (12 mg ml^{-1}) the spacing is decreased to ≈20 μm with several bridges connecting the lamellae. Further investigation and discussion of bidirectional freeze-casting mechanisms can be found in [73].

Freeze-casting techniques have proven to be efficient and versatile ways of processing and manipulating 3D macroporous architectures of MXenes, but they still lack deeper and systematic investigation of the fundamental mechanisms. For example, more research needs to be done into the impact of functional group distribution on the surface of MXenes, as these are likely to have a measurable effect on their gelation capability and assembly during freezing. The technique could also favor from further investigation of different solvents and more elaborated freezing set-ups to manipulate pores size and shape in practical sizes (beyond a few cm). Finally, the establishment of process-structure-property relationships would benefit from the coupling of processing with advanced structural characterization techniques (e.g. microCT) and modeling, which would help establish the fundamental mechanisms during freeze-casting. For a fundamental discussion and understanding of freezing

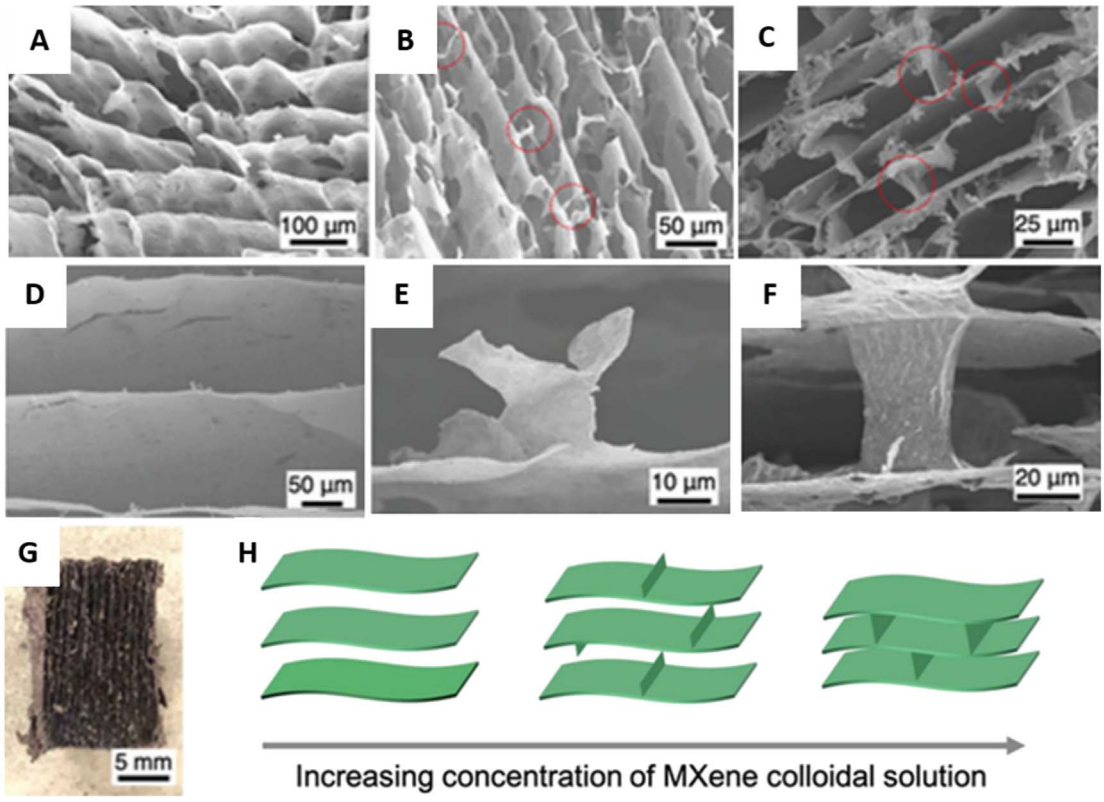

Figure 8. Structure and morphology of lightweight $Ti_3C_2T_x$ aerogels by bidirectional freeze-casting with aligned lamellar structure and different densities. SEM images of $Ti_3C_2T_x$ aerogels with (A) 5,5, (B) 8,3, and (C) 11 mg cm^{-3}, respectively. Interlayer synapses and bridges are circled in red. Magnified SEM images of (D) 5,5, (E) 8,3, and (F) 11 mg cm^{-3} $Ti_3C_2T_x$ aerogels showing the layer spacing and interlayer structure. (G) Digital image of free-standing $Ti_3C_2T_x$ aerogel showing the oriented structure on the centimeter scale. (H) Schematic illustration shows the decreasing interlayer spacing and formation of interlayer 'bridges' in freeze-dried MXene aerogels from MXene colloidal solutions with increasing concentration [70]. [70] John Wiley & Sons. [© 2019 WILEY-VCH Verlag GmbH & Co. KGaA, Weinheim].

colloidal suspensions the reader should refer to *Freezing Colloids: Observations, Principles, Control and Use* by Deville [74].

4.3.3. Alternative template-assisted techniques

Besides using the ice growth interface, there have been a few attempts to create macroscopic 3D structures with different template assisted techniques [75–77]. In 2015, Hu *et al* reported the drop casting of a $Ti_3C_2T_x$ suspension into a Ni foam template, forming a MXene film which exhibited high gravimetric capacitance [75]. Although this work maintains the metallic framework, depending on the necessity, it could potentially be removed through chemical etching to form a free-standing 3D MXene architecture similar to the process already employed for graphene-based 3D materials. Also, high-performance and flexible volatile organic compounds sensors based on 3D MXene framework (3D-M) were prepared by immersing an electrospinning produced PVA/PEI 3D framework into MXene dispersion for several minutes and subsequently drying it in air [77].

Bian *et al* [76] proposed the assembly of $Ti_3C_2T_X$ directed by water/oil interfaces. By tuning the MXene hydrophilicity *via* the exchange of H^+ with a cationic surfactant, such as cetyltrimethylammonium bromide (CTAB), on the –OH groups, they show that it is possible to prepare high internal phase emulsions (HIPEs). These emulsions' stability is shown to be highly dependent of the solutions pH. Further temperature-initiated polymerization of the binder results in the formation of a porous monolith with a cellular structure.

Another interesting templating method was recently proposed by Pan *et al* who built all-solid-state supercapacitors (ASSS) [78]. In this work, an accordion-like etched MXene is dispersed in PMMA and successively sprayed on the surface of 6 μm thick copper foil. The coated foils were then stacked, hot pressed and subsequently cut perpendicular to the layered direction by electric spark machining. Finally the 500 μm thin

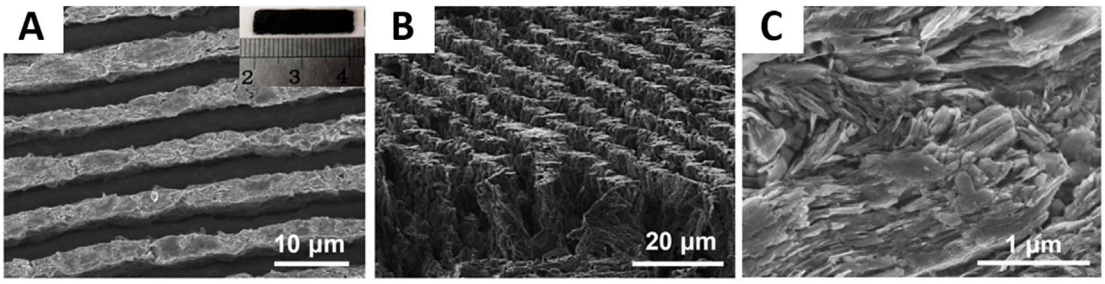

Figure 9. (A) Top and (B) side viewed SEM images of hierarchical MXene array structure. (C) SEM image of fine structure of MXene accordion after hot-pressing [78]. Reprinted with permission from [78]. Copyright (2019) American Chemical Society.

sheets were treated with ammonium persulfate on one side to etch the Cu template to a certain height, forming an ordered MXene array as shown in figure 9.

In 2015, Xu *et al* reported for the first time a bottom-up approach of producing large-area, high quality, ultrathin Mo_2C MXenes using chemical vapor deposition (CVD) [79], other transition metal carbides and nitrides (such as WC, TaC, TaN, MoN), and heterostructures have also been obtained in similar processes. As highlighted by Verger *et al* [10], it is important to note that none of these methods were able to produce single layer materials. Synthesis of MXenes by CVD and other bottom-up approaches are still very much unexplored, however, as one of the most common techniques of building high quality 3D graphene scaffolds [2, 80], these works present promising potential for the processing of high-quality 3D MXene architectures for specific applications.

4.3.4. Additive manufacturing

Additive manufacturing (AM), in contrast to the previously discussed techniques, follows designed computer models to build structures layer by layer. This brings advantages in shape and structural control, opening opportunities to print integrated components, improve cost effectiveness and automation. In particular, techniques that are based on the deposition of inks (direct ink writing, DIW), can assemble materials of different chemistry and dimensionality into 3D complex architectures. DIW of 3D structures is particularly effective when using extrusion-based 3D printing approaches (e.g. robocasting) [81]. The first step of robocasting is the formulation of colloidal inks with specific rheological properties that ensure smooth flowing under high shear stress to facilitate the extrusion of materials during printing and adequate resistance to deformation under low shear stress to retain the shapes and structures of as-printed objects.

Since the first demonstrations of the 3D printability of GO [82], numerous studies on printing graphene-based inks have been reported and reviewed [2, 83, 84]. It has been shown that high aspect ratio materials with surface charges like clay, GO and MXenes are particularly effective at tuning the rheological properties and processability of colloidal inks [85, 86]. In particular, the highly negatively charged surfaces and more positive edges of MXenes gives them electrostatic and intercalation properties similar to some clays creating useful rheological properties for colloidal processing [17, 87]. Akuzum *et al* reported a systematic investigation into the rheological properties of $Ti_3C_2T_x$ aqueous suspensions to establish guidelines to explore and select concentration and operation conditions for different processing routes (from electrospray to extrusion printing) (figure 10) [85]. They proposed that single- and multilayer MXenes should be considered as two different colloidal systems, as they were found to exhibit very different viscous and viscoelastic properties at different concentration regimes. Viscosity measurements have shown shear-thinning behavior with visible flowability for multilayer MXenes even at the highest tested loading (70 wt%). On the other hand, dispersions of single-layer $Ti_3C_2T_x$ have shown an early spike in viscosity at concentrations of around 1 mg ml^{-1} (*ca.* 0.1 wt%). The authors argue that the elastic component present at really low concentrations is due to strong surface charge (−45.9 mV), lower packing density, and hydrophilicity of MXene.

Although Akuzum *et al* study provides insights into the processability of MXenes, the development of printing procedures and ink formulations are still at the early stages; mostly producing flat re-stacked films or single printed layer arrays using techniques such as painting, writing [88], stamping [89], screen printing [90, 91] and extrusion [92] and hence not fully utilizing the potentialities of printing in three-dimensions.

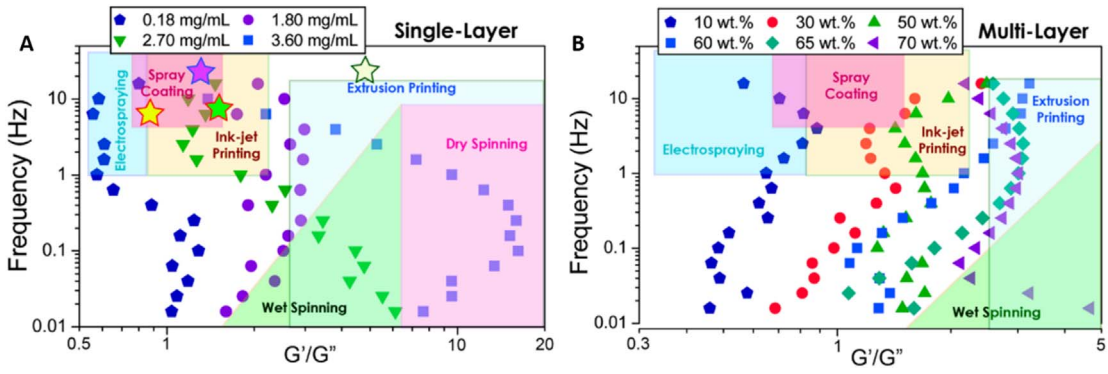

Figure 10. (A) Frequency dependency of the ratio of the G′ elastic modulus to G″ viscous modulus for single-layer $Ti_3C_2T_x$ MXene flakes dispersed in water. (The superimposed stars on the plot represent the approximate processing parameters used in different applications of MXenes from the literature.) (B) Frequency dependency of the ratio of the G′ elastic modulus to G″ viscous modulus for multilayer $Ti_3C_2T_x$ MXene particles dispersed in water [85]. Reprinted with permission from [85]. Copyright (2018) American Chemical Society.

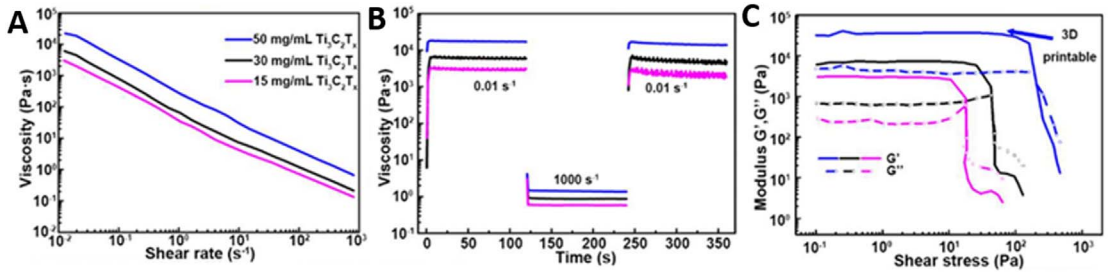

Figure 11. (A) Inks shear thinning behavior for continuous extrusion through printing nozzles with 250 μm diameter. (Inset legend refers to line colors used in panels (A)–(C). (B) Inks viscosity evolution over time for alternate low (0.01 s^{-1}) and high shear rate (1000 s^{-1}). (C) Inks viscoelastic fingerprints [93]. [93] John Wiley & Sons. [© 2019 WILEY-VCH Verlag GmbH & Co. KGaA, Weinheim].

Only recently Yang *et al* demonstrated for the first time the possibility to print 3D MXene freestanding objects by designing inks composed solely of large, high aspect ratio MXene flakes (8 μm average lateral size and 1–3 layers) and water [93]. The inks were specifically formulated and characterised to probe their printability in 3D. Additive-free aqueous inks with 1.5, 2.9 and 4.8 wt% $Ti_3C_2T_x$ showed appropriate shear thinning behavior for continuous extrusion through printing nozzles as narrow as 250 μm diameter (figure 11(A)). The inks viscosity evolution over time for alternate low (0.01 s^{-1}) and high shear rate (1000 s^{-1}) also showed appropriate viscosity drop and post-printing recovery (figure 11(B)). The viscoelastic fingerprints showed their solid-like behavior with large plateau regions (where G′ is independent of stress) and yield stresses (cross over point between G′ and G″) that increase as the inks become more concentrated. In particular, it is shown that inks at 4.8 wt% MXene present an elastic modulus of 3747 Pa and extendable plateau regions with a yield stress of 206 Pa enabling them to be 3D printable (figure 11(C)). After printing, the materials were subsequently freeze dried to generate 3D printed structures with internal porous microstructure. Figure 12 shows printed multiscale architectures achieved by this method and their respective hierarchical microstructure.

Later, Yu *et al* designed crumpled N-doped MXene (MXene-N) composite inks for printable electrochemical energy storage devices [91]. By mixing MXene-N with carbon nanotubes (CNT), activated carbon (AC) and GO, they were also able to produce a highly viscous, binder-free hybrid ink with ideal shear-thinning features for extrusion printing with controlled thickness. These reports shed light on the huge potential that MXene-based inks present for 3D printing.

Although not directly related to printable ink formulations, the recent work of Deng *et al*, discussed in section 4.3.1, showing cation-induced gelation of MXene hydrogels [54], introduces another promising way of developing MXene-based inks with desirable rheology, with the possibility of using additives that can actually tune and enhance their electrochemical properties after processing. A cation-induced gelation with

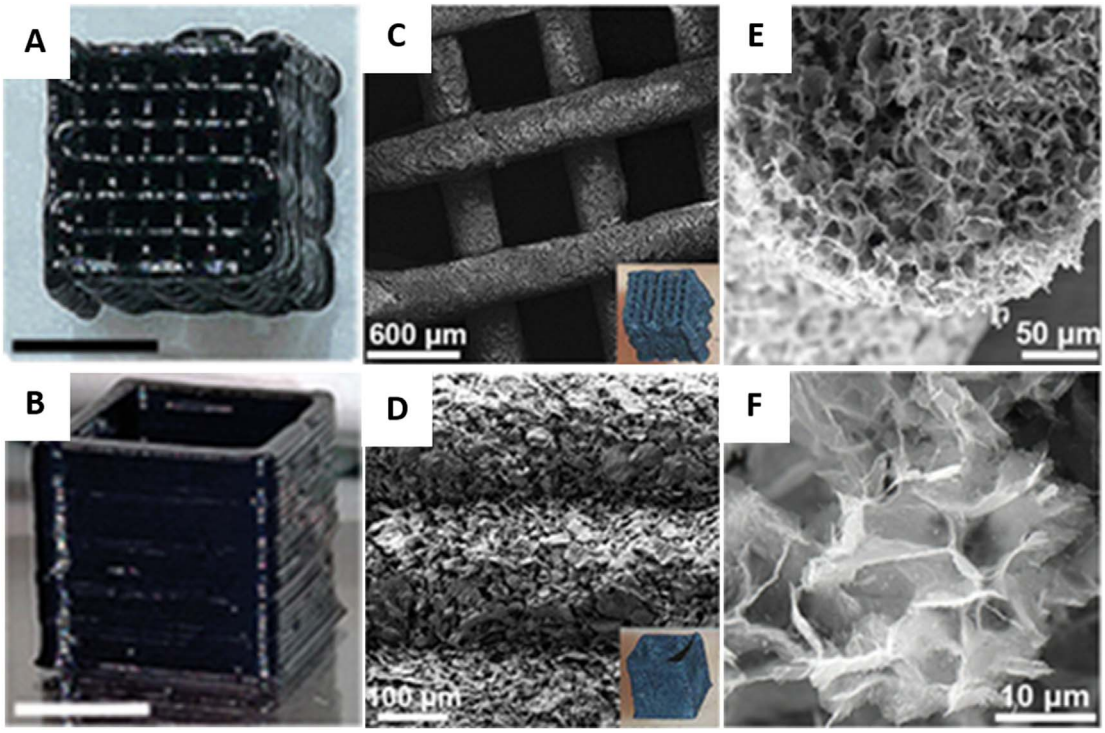

Figure 12. 3D printed multiscale architectures after freeze-drying. (A) and (B) Digital images of 3D printed different architectures showing their height and shape retention (scale bars: 3 mm). (C) and (D) SEM and digital images (inset) of freestanding $Ti_3C_2T_x$ microlattice and hollow rectangular prism printed through 330 and 250 μm nozzles, respectively. (E) and (F) Cross-sectional SEM images of one filament within the microlattice show the retention of shape and formation of porous internal structures upon freeze-drying [93]. [93 John Wiley & Sons. [© 2019 WILEY-VCH Verlag GmbH & Co. KGaA, Weinheim].

trace addition of Ca^{2+} ions was already successfully demonstrated to directly print self-standing graphene aerogel microlattices from GO-based ink and this approach could be a good base to explore MXene-based inks [94].

5. Characterization of porous architectures

Some of the key properties to characterize 3D porous architectures and aerogels include: true, apparent and bulk densities (density of the solid material forming a structure without considering pores, considering the volume of closed pores, and considering the volume of open and closed pores, respectively); total and effective porosities (volume of pores per bulk volume of the structure, and just open pores per bulk volume, respectively); specific surface area; surface roughness; and pore morphology and distribution.

Several techniques can be used to assess these properties, such as geometrical measurements, liquid and powder immersion, mercury porosimetry, pycnometry, capillary flow porometry, fluid flow, gas sorption, calorimetric determination, microscopy (optical, SEM, TEM), and x-ray computed tomography (microCT) [95–98]. The applicability of these techniques will depend on the materials present, and the physical properties of the sample, such as surface characteristics, pore size range, and pore morphology. Many of the methods use models to determine the porosity parameters and these will take into account an ideal geometry which might not be a good representation of the samples being tested. All this needs to be taken into account when translating the knowledge and good practice developed in other materials classes (such as porous ceramics or polymers) to 2D materials based aerogels.

To assess the density of a material, measuring the volume of a 3D porous structure can be tricky due to their shape complexity and typically rough surface. Water immersion (Archimedes method) is the typical approach to measure apparent volume of materials as it covers the entire structure and penetrate open pores. However, depending on the roughness and hydrophobicity of the porous structure, this method may overestimate the apparent volume, and in the case of architectures held together solely by van der Waals forces (typical for 2D materials), the water may also destroy the sample. The Archimedes method can also be used to determine the bulk density of a sample by covering it with a sealant to prevent infiltration of the open pores, but the sealant volume might be a large source of error if the samples are too small or light. Powder immersion is a good alternative for measuring the bulk volume, as long as the powder particles have an average size larger than the

open pores. Meanwhile, gas pycnometry can measure the true or the apparent density of the solid phase, depending on whether or not the gas molecules are able to penetrate the closed pores. Despite the classification we use for the density of structures, other nomenclatures exist, so we strongly suggest that regardless of the used terminology, the method and the proportion of voids taken into account are described.

The total porosity of a structure is given by the volume of pores as a fraction of the bulk volume of the whole structure. This can be found by using the previous methods of measuring the true, apparent and bulk volumes of materials. Also, mercury porosimetry and capillary flow porometry, and gas sorption can be used to directly determine porosity, pore size distribution, and surface area.

Since one of the main incentives to assemble 2D materials into 3D porous structures is to prevent restacking and increase the available specific surface area, gas sorption and Brunauer–Emmett–Teller (BET) analysis are commonly applied in research, but several issues must be taken into account that are frequently ignored or overlooked. The BET method estimates the specific surface area through the physical adsorption of gas molecules on a solid surface, but it is well known that the BET equation does not apply to microporous adsorbents [99]. ISO 9277:2010, for example, specifies the determination of the overall specific surface area of disperse (e.g. nanopowders) or porous solids, but is only applicable to adsorption isotherms of *type* II (disperse, nonporous or macroporous solids) and *type* IV (mesoporous solids, pore diameter between 2 and 50 nm) [100]. The results can also become unreliable if the material absorbs the measuring gas. MXenes also bring, as discussed, a variety of compositions and different termination groups that are not evenly distributed over their surfaces [27, 28], and this might interfere with the gas sorption mechanisms. Bearing this in mind, the BET surface area should never be taken at face value when characterising nanostructured, 2D-based materials—especially MXenes. The reader is advised to refer to [99] for a deeper discussion on how BET, allied with calorimetry, can be used to provide reproducible and meaningful information about microporous materials.

Although microscopy observations are the main way to assess the morphology and size distribution of pores and particles, it is often only used for qualitative assessment. Also, some structures might be more sensitive to processing parameters than others. For example, besides the expected directional anisotropy, pores of freeze-cast samples can also be inhomogeneous—varying in different ways across the sample depending on the processing conditions. Monoliths made by unidirectional freeze-casting tend to have a region of smaller and less ordered pores near the cold finger above which the lamellar structures start to form, and subsequently have larger pores at greater distances [64, 74]. For that reason, when fracturing freeze-cast samples for crossectional analysis, it is important to record the region of the sample depicted in micrographs, and the direction of the fracture.

The constant improvements in resolution and capabilities of microCT make it a powerful, nondestructive alternative to microscopy, that provides accurate data for dimensional measurement and porosity analysis throughout the entire structure [98]. However, the small sample sizes necessary to achieve high resolution mean that analysis is limited by the assumption that results would be similar in larger samples, and therefore it should always be done in combination with microscopy. It is also important to consider that 2D materials are capable of forming porous structures with walls less than 10 nm thick, which is far below the resolution achieveable by current microCT technologies (~100 nm), and so the thickness of these walls will be overestimated.

In summary, no experimental method provides the absolute value of a measured property (such as porosity, surface area, pore size, or surface roughness), but gives a characteristic value that depends on the principles employed to perform the measurement. Therefore, one must be aware of the limited and complementary significance of the information delivered by each method of characterization. Further, studies should also evaluate the properties of the MXene flakes (such as degree of oxidation, functional groups ratio, interlayer spacing, and even morphology) after the fabrication of 3D architectures. This will allow a better understanding of the effect of processing on the MXene properties. Table 1 summarizes the main reviewed processing methods for 3D porous structures with specific data provided by the respective references.

6. Electrochemical energy storage

A number of different electrode architectures have been proposed for energy storage devices as shown in figure 13. As discussed in further detail by Sun *et al* [102], the oldest design comprises anode and cathode plates divided by a porous membrane separator and infiltrated with a liquid electrolyte (figure 13(A)). For charging and discharging, ions must travel between cathode and anode through the electrolyte across the whole thickness of the device. The ion diffusion time in this process is one of the main limitations to rate performance. Stacked thin films and interdigitated (figures 13(B) and (C)) electrodes help to reduce the ion diffusion length enabling faster charge delivery for high-power applications. However, these are usually limited to planar geometries and micrometric scales. 3D designs such as the 3D tri-continuous electrode assembly as proposed by Werner *et al*

Table 1. Summary of 3D porous structures processing methods.

	Processing method	Particle/pore morphology	References	Composite materials	Investigated applications	Notes on processing and structure
3D Nanostructured Particles	Low concentration sol freeze-Drying	Crumpled particles	[53]	$Ti_3C_2T_x$	—	
	Sacrificial template	Hollow Spheres	[40]	$Ti_3C_2T_x$ Mo_2CT_x V_2CT_x	—	Sacrificial Templates: PMMA spheres Particles Size: $\approx$ 2–3 μm (SEM) tunable by template size
			[13]	$Ti_3C_2T_x$ Mo_2CT_x	—	Sacrificial Templates: PMMA spheres Particles Size: $\approx$ 1.1 μm (SEM) tunable by template size
	Spray drying	Crumpled Particles	[41]	$Ti_3C_2T_x$	—	This work claims the crumpled morphology is partially reversible when hydrated
			[45]	$Ti_3C_2T_x$	Water Splitting	Particles Size: $\approx$ 0.5–3.5 μm (tunable by MXene concentration 0.5–5.0 mg ml^{-1}) SSA: 165.3 m^2 g^{-1} (N_2 sorption)
	Alkali/Acid treatment	Crumpled Particles	[42]	N-$Ti_3C_2T_x$/S	Li–S Batteries	BET SSA: 385 m^2 g^{-1} (N_2 sorption) BET Pore volume: 0.342 cm^3 g^{-1} (N_2 sorption) BET Pore size: 15–80 nm (N_2 sorption) N-doping made by thermal annealing of MXene and melamine. Mixing crumpled N-$Ti_3C_2T_x$ with 74 wt% molten sulfur achieved homogeneous coating of the particles
			[43]	$Ti_3C_2T_x$	Na-Ion Batteries	BET SSA: 21.4 m^2 g^{-1} (N_2 sorption) BET Pore size: 4 nm, 20 nm, 60 nm (N_2 sorption) Pore size: 100–400 nm (SEM) Large, crumpled flocs generated in alkaline solvent
			[44]	$Ti_3C_2T_x$	Na-Ion Batteries	BET SSA: 33 m^2 g^{-1} (N_2 sorption) BET Pore size: 3–5 nm (N_2 sorption) Large, crumpled flocs generated in acid solvent
		Narrow Nanoribbons	[46]	$Ti_3C_2T_x$	Na/K-Ion Batteries	Nanoribbons width: 6–22 nm Nanoribbons thickness: $\approx$ 27 nm BET SSA: 25 m^2 g^{-1} (N_2 sorption) Nanoribbon network formed by shaking multilayer MXenes in KOH

Table 1. (Continued.)

	Processing method	Particle/pore morphology	References	Composite materials	Investigated applications	Notes on processing and structure
			[47]	$Ti_3C_2T_x$/S	Li–S Batteries	Mixing alkalized nanoribbons with 68 wt% molten sulfur achieved homogeneous coating of the nanoribbons
	Fluorine-free hydrothermal synthesis	Wide Nanoribbons	[35]	$Ti_3C_2(OH)_2$	—	Nanoribbons width: 200–400 nm Nanoribbons thickness: ≈ 27 nm The morphology is formed during the synthesis and can also produce rod-like and slab-like particles.
	Slurry of crumpled particles	—	[53]	$Ti_3C_2T_x$/Carbon Black	Capacitive Desalination	BET SSA: 293 $m^2\ g^{-1}$ (N_2 sorption) BET Pore volume: 0.327 $cm^3\ g^{-1}$ (N_2 sorption) BJH Pore size: 15–40 nm (N_2 sorption)
	Vacuum filtration of pre-made 3D nanostructured particles	Hollow spheres	[40]	$Ti_3C_2T_x$ Mo_2CT_x V_2CT_x	Na-Ion Batteries	Films thickness: 13 μm Pores sizes: ≈ 2–3 μm Water contact angle: 135° Densities: 0.4 g cm^{-3}
			[13]	$Ti_3C_2T_x$ Mo_2CT_x	Supercapacitors	Films Thickness: 13–180 μm Pores sizes: ≈ 1.1 μm Densities: 0.25–0.4 g cm^{-3}
3D Porous Films	Vacuum filtration of mixture of 2D MXene with 1D bacterial cellulose fibers	Cellular pores	[101]	$Ti_3C_2T_x$/Bacterial Cellulose	Supercapacitors	
	Hydrazine treatment of compact film		[51]	$Ti_3C_2T_x$	EMI Shielding, Organic Absorption	Films thickness: 6–60 μm (SEM) Densities: 0.22–0.40 g cm^{-3}
			[52]	Ti_3C_2/rGO	Li-Ion Batteries	Films Thickness: 18–48 μm (SEM) BET SSA: 39.86–72.98 $m^2\ g^{-1}$ (N_2 sorption)

Table 1. (Continued.)

	Processing method	Particle/pore morphology	References	Composite materials	Investigated applications	Notes on processing and structure
	Induced gelation followed by freeze-drying	Cellular pores	[55]	$Ti_3C_2T_x$	Supercapacitors	Functionalisation: EDA Sample thickness: >1 mm BET SSA: 176.3 $m^2\ g^{-1}$ (N_2 sorption) Pore volume: 3–5 nm and 5–10 nm (N_2 sorption) Radially oriented porosity
			[56]	N-$Ti_3C_2T_x$	Supercapacitors	Functionalisation: Thiox and Ammonia BET SSA: 108 $m^2\ g^{-1}$ (N_2 sorption) BJH Pore volume: 2.9–8.2 nm (N_2 sorption) Densities: $\approx$ 27 mg cm^{-3}
			[57]	$Ti_3C_2T_x$/PI	EMI Shielding, Thermal Insulation	Cross-linker: PAA Porosities: 99.3–98.0%. Densities: 10.7–27.9 mg cm^{-3} Reversible Compress/Stretchability: 80/20%
			[54]	$Ti_3C_2T_x$	Supercapacitors Organic Absorption (SI)	Cross-linker: Divalent Metal Ions ($\square^{2+}$) SSA: 27 $m^2\ g^{-1}$ (N_2 sorption) for sample with Fe^{2+} as cross-linker
3D Porous Macrostructures	Uncontrolled freeze-casting		[71]	$Ti_3C_2T_x$	EMI Shielding, Organic Absorption	Sample thickness: > 1 cm Pore size: $\approx$ 20 μm (SEM) Densities: 0.004–0.021 g cm^{-3}
	Water/oil emulsion templating		[76]	$Ti_3C_2T_X$	—	Samples thickness: $\leqslant$ 1 cm Pore size: $\approx$ 65–200 μm (SEM) Porosity: $\approx$ 70%
	Unidirectional freeze-casting	Long highly oriented pores	[61]	Ti_3C_2/rGO	EMI Shielding	Samples thickness: 2 mm Densities: 0.024–0.044 g cm^{-3}
			[72]	$Ti_3C_2T_x$	Supercapacitors	Samples thickness: 10 mm Lamellae spacing: $\approx$ 32–53 μm (SEM) Porosities: 99.2–99.8% Densities: 0.007 to 0.043 g cm^{-3} BET SSA: 30.122 $m^2\ g^{-1}$ (N_2 sorption) BJH Pore size : 1.580 nm (N_2 sorption)

Table 1. (Continued.)

Processing method	Particle/pore morphology	References	Composite materials	Investigated applications	Notes on processing and structure
Unidirectional freeze-casting, pressing and calendering					Samples thickness: 0.06–0.17 mm Lamellae spacing: $\approx$ 1–2 μm (SEM) Porosities: 72.5–90.0% Densities: 0.375–1.030 g cm^{-3} BET SSA: 39.831 m^2 g^{-1} (N_2 sorption) BJH Pore size : 1.580 nm (N_2 sorption)
Bidirectional freeze-casting		[73]	Ti_2CT_x $Ti_3C_2T_x$ Ti_3CNT_x	EMI Shielding	Samples thickness: $>$ 1 mm Lamellae spacing: $\approx$ 20–150 μm (SEM) Densities: 0.0055–0.011 g cm^{-3}
Copper sacrificial templating	Vertical array structures	[78]	$Ti_3C_2T_x$ on Cu	Supercapacitors	Etched array height: 5–50 μm (SEM) Layers thickness: $\approx$ 5 μm (SEM) Layers spacing: $\approx$ 6 μm (SEM)
Extrusion 3D printing and freeze-drying	Multiscale architectures with crumpled pore walls	[93]	$Ti_3C_2T_x$	Supercapacitors	Filament diameter: 250–330 μm (SEM) Pore size: 3–35 μm (SEM) SSA: 177 m^2 g^{-1} (N_2 sorption) DFT Pore size: 0.8–9 nm (N_2 sorption)
		[91]	AC/CNT/N-$Ti_3C_2T_x$/GO	Supercapacitors	BET SSA: 234.1 m^2 g^{-1} (N_2 sorption) DFT Pore volume: 0.265 cm^3 g^{-1} (N_2 sorption)

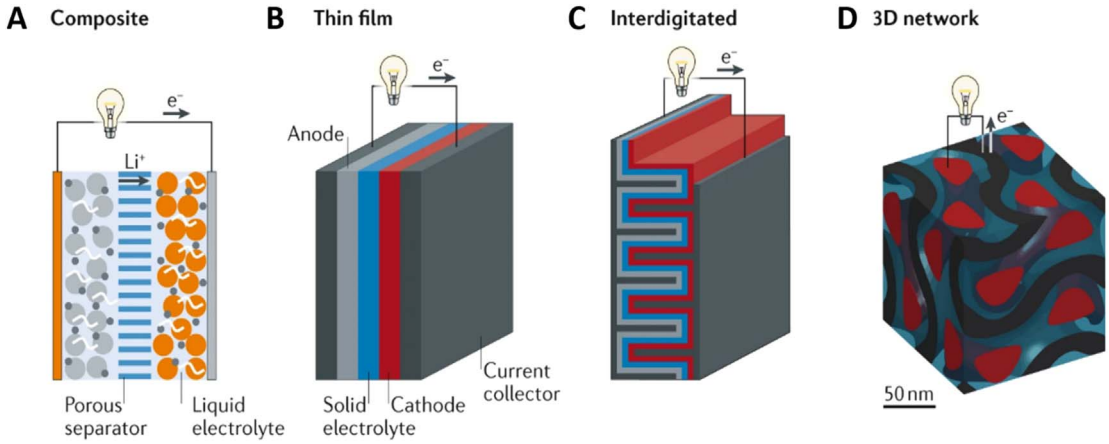

Figure 13. Schematics of different battery architectures. Typical (A), thin-film (B), interdigitated thin-film (C), and 3D tri-continuous nanolayer designs (D) [102]. Reprinted by permission from Springer Nature Customer Service Centre GmbH:] [Nature Reviews Materials].

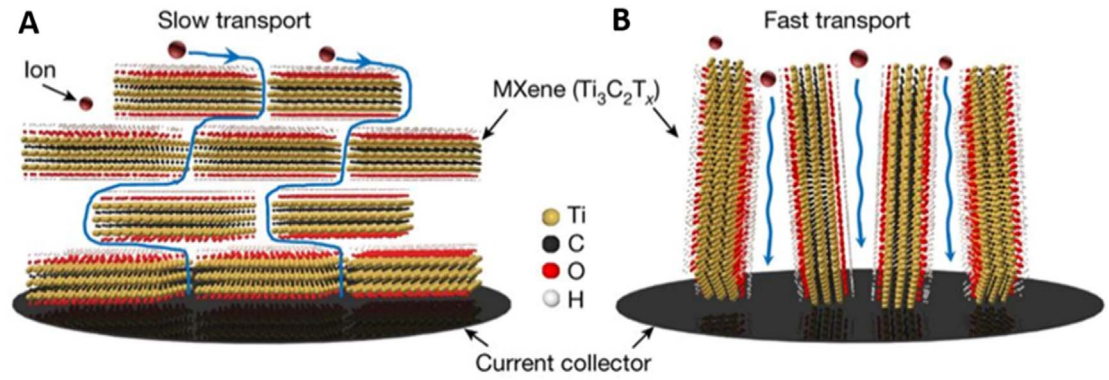

Figure 14. Schematic illustration of ion transport in $Ti_3C_2T_x$ MXene films. (A) Ion transport in horizontally stacked and (B) vertically aligned $Ti_3C_2T_x$ MXene films. The blue lines indicate ion transport pathways [106]. Reprinted by permission from Springer Nature Customer Service Centre GmbH: [Nature].

[103] allows the integration of the nanometric components in a 3D architecture improving their power capability without negatively impacting the energy density.

Since their first publication, MXenes have shown great potential for use as electrodes in energy storage devices due to their unique structure, which combines the conductivity of transition metal carbide layers with an oxygenated surface that provides redox active sites and allows water intercalation for improved ion transport [8, 13]. However, in order to fully utilise their potential it is important that individual MXene layers remain fully accessible, so that ions can easily diffuse between the adsorptions sites. To date, the majority of MXene electrodes researched are fabricated using simple methods such as slurry processing or filtration, but these traditional techniques will not necessarily lead to optimised electrodes since multiple layers get stacked hindering ion mobility and accessibility [104, 105]. Xia *et al* [106] have shown, for example, that the alignment of MXene flakes can be used to increase ion diffusion rate in a chosen direction (figure 14), enabling the output of supercapacitors to become thickness independent up to *ca*. 200 μm. Further, by assemblying MXenes into 3D structures with high effective porosity the specific surface area can be increased from 4 to 55 $m^2\ g^{-1}$ (typical of compact films made using traditional methods) to 177 $m^2\ g^{-1}$ (in 3D printed MXene) [93].

Moreover, MXenes generally have a very negative ζ-potential (-30 to -80 mV) thanks to their functional groups (e.g. O, F and OH) [9], which allows strong interaction with electrolytes, and positively charged materials with which they can form nanocomposites and heterostructures. As a porous matrix, 3D MXenes can then accomodate large volume changes in electroactive nanomaterials which often exhibit poor cycle lifetimes due to intercalative swelling-shrinkage during charge–discharge cycles.

6.1. Batteries

Since the development of the delaminated $Ti_3C_2T_x$ paper electrode in 2013 [105], the majority of work into novel MXene-based battery electrodes has sought to develop high capacity, high power composites for Li-ion

Table 2. Capacity properties of MXene-based 3D porous architectures as electrodes for batteries.

References	Electrode material	Electrode morphology	Ion	Capacity (mAh g^{-1})	Rate	Notes
[105]	Exfoliated $Ti_3C_2T_x$		Li-ion	110	36 C	Measured after 120 cycles at 1 C and 750 cycles at 36 C
		Compact film				
				410	1 C	
[98]	*m*-$Ti_3C_2T_x$		Li-ion	203	0.2 A g^{-1}	Dropped and regained after 500 cycles
[33]	*m*-$Ti_3C_2T_x$		Na-ion	175	20 mA g^{-1}	
				60	5 A g^{-1}	
[42]	$Ti_3C_2T_x$/S		Li–S	585	0.2 C	S loading 5.1 mg cm^{-2}
				418	2 C	
[44]	Cl-c-$Ti_3C_2T_x$	Crumpled Particles	Na-ion	120	0.5 A g^{-1}	Retained after 50 cycles
				250	20 mA g^{-1}	
[43]	Li-c-$Ti_3C_2T_x$		Na-ion	238	1.0 A g^{-1}	69% retained after 300 cycles at 0.1 A g^{-1}
				157	0.1 A g^{-1}	
	Na-c-$Ti_3C_2T_x$		Na-ion	61	1.0 A g^{-1}	Stable for 300 cycles at 0.1 A g^{-1}
				130	0.1 A g^{-1}	
	K-c-$Ti_3C_2T_x$		Na-ion	97	1.0 A g^{-1}	Stable for 300 cycles at 0.1 A g^{-1}
				45	0.1 A g^{-1}	
[42]	c-N-$Ti_3C_2T_x$/S		Li–S	610	2 C	S loading 5.1 mg cm^{-2}
				1144	0.2 C	
[110]	$Na_{0.23}TiO_2/Ti_3C_2$	Composites	Li-ion	178	5 A g^{-1}	Measured after 4000 cycles
[48]	MoS_2/Ti_3C_2@C		Li-ion	580	20 A g^{-1}	95% retained after 3000 cycles
				1130	0.2 A g^{-1}	
[109]	CNTs@Ti_3C_2		Li-ion	175	10 A g^{-1}	Retained after at least 500 cycles
				430	1 A g^{-1}	
[35]	$Ti_3C_2(OH)_2$	Nanoribbons	Li-ion	120	0.1 A g^{-1}	Increased to 143 mAh g^{-1} after 250 cycles
[46]	a-$Ti_3C_2T_x$		K-ion	60	0.3 A g^{-1}	60% retained after 500 cycles
				141	20 mA g^{-1}	
			Na-ion	85	0.3 A g^{-1}	25% capacity lost between 25th and 500th cycles
				167	20 mA g^{-1}	
[47]	a-$Ti_3C_2T_x$/S		Li–S	288	10 C	S loading 0.7–1 mg cm^{-2}
				632	0.5 C	
[40]	ho-Mo_2CT_x	Hollow Spheres Film	Na-ion	370	50 mA g^{-1}	Increased 38% after 1000 cycles at 0.5 A g^{-1}
				130	5 A g^{-1}	
[40]	ho-$Ti_3C_2T_x$		Na-ion	330	50 mA g^{-1}	Increased 40% after 1000 cycles at 0.5 A g^{-1}
				124	5 A g^{-1}	
[40]	ho-V_2CT_x		Na-ion	340	50 mA g^{-1}	Increased 20% after 1000 cycles at 0.5 A g^{-1}
				174	5 A g^{-1}	
[52]	Ti_3C_2/rGO	Macroporous Composite Foam	Li-ion	99	4 A g^{-1}	Increased 20% after 1000 cycles
				336	50 mA g^{-1}	

and Li–S batteries, and to improve the performance of other metal-ion batteries containing larger ions such as Na^+ and K^+ [107]. 3D porous architectures fabricated for these purposes have predominantly been processed using similar methods to those presented in sections 4.1 and 4.2, where the 2D flakes are assembled into 3D particle morphologies and subsequently vacuum filtered to form low-density films with macroporosity. To date, the studied morphologies fall into four major categories: nanoribbons [46, 47], crumpled particles [42, 44, 108], composites [48, 49, 109, 110], and pore modified films [40, 52, 111]. The performances of selected electrodes are summarized in table 2.

Since discovering that compacting $Ti_3C_2T_x$ flakes inhibits the performance of fabricated electrodes [105, 112], Barsoum *et al* investigated the benefits of exploiting a crumpled flake morphology [44, 108]. It was

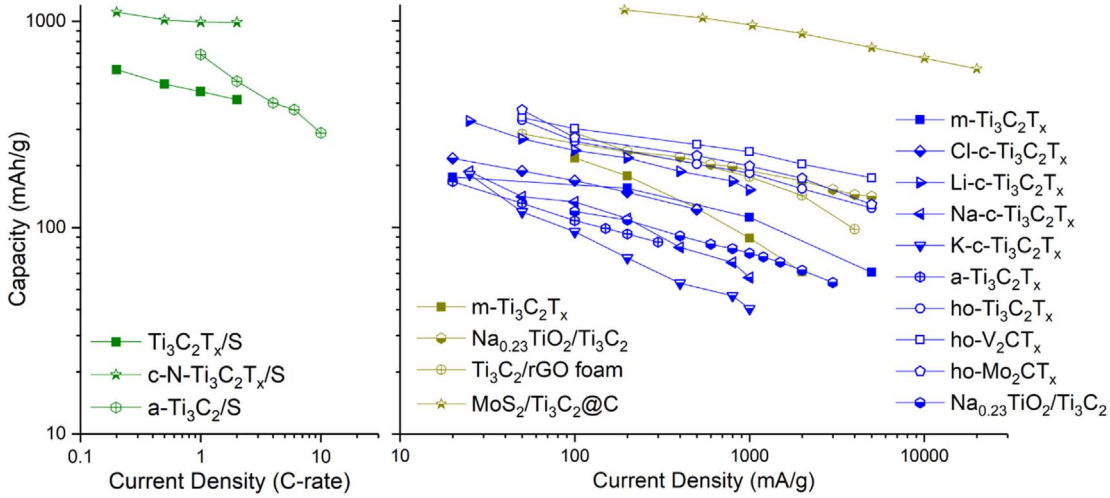

Figure 15. Current density *versus* capacity of meso- and macroporous MXene-based anodes for Li–S (green), Li-ion (yellow) and Na-ion (blue) batteries. The list includes unmodified $Ti_3C_2T_x$/S and crumpled nitrogen-doped $Ti_3C_2T_x$/S (c-N-$Ti_3C_2T_x$/S) [42]; alkalised Ti_3C_2/S nanoribbons (a-Ti_3C_2/S) [47]; multilayer $Ti_3C_2T_x$ (m-$Ti_3C_2T_x$) [40, 115]; $Na_{0.23}TiO_2/Ti_3C_2$ [110]; MoS_2/Ti_3C_2@C [48]; Ti_3C_2/rGO foam [52]; crumpled $Ti_3C_2T_x$ made by suspension in HCl (Cl-c-$Ti_3C_2T_x$) [44], LiOH (Li-c-$Ti_3C_2T_x$), NaOH (Na-c-$Ti_3C_2T_x$), or KOH (K-c-$Ti_3C_2T_x$) [43]; alkalised $Ti_3C_2T_x$ (a-Ti_3C_2) nanoribbons [46]; and hollow spheres of $Ti_3C_2T_x$ (ho-$Ti_3C_2T_x$), V_2CT_x (ho-V_2CT_x), and Mo_2CT_x (ho-Mo_2CT_x) [40]. Li-ion and Na-ion batteries data were adapted from [107]. [107 John Wiley & Sons. [© 2019 WILEY-VCH Verlag GmbH & Co. KGaA, Weinheim].

found that when using $Ti_3C_2T_x$ that had been crumpled (c-$Ti_3C_2T_x$) *via* the introduction of strong acid or alkali (HCl, NaOH, or KOH), anodes had *ca*. 10 times the Na capacity achieved using delaminated $Ti_3C_2T_x$, or over 20 times when LiOH was used as the crumpling agent (Li-c-$Ti_3C_2T_x$). In the study on alkali-induced crumpling, it was determined that the use of MXene crumpled with NaOH (Na-c-$Ti_3C_2T_x$) or KOH (K-c-$Ti_3C_2T_x$) produced electrodes with a lower initial capacity, but much better cycling stability than the equivalent electrode made with Li-c-$Ti_3C_2T_x$. The reason for the difference in initial capacity is uncertain, but the improvement in cycling stability is thought to be due to the 'pillaring effect' of trapped Na^+/K^+ ions working synergistically with the porous structure to prevent flake restacking—maintaining ion accessibility—and reduce intercalative volume changes.

In the case of lithium–sulfur (Li–S) batteries, MXenes serve to act as a conductive scaffold for sulfur-based cathodes [42, 47]. While Li–S batteries are desirable because of their high capacity and low cost (figure 15), there is an ongoing challenge to fabricate electrodes which do not suffer from poor rate performance due to the low conductivity of sulfur, and poor cyclability due to cathode volume expansion and 'the shuttling effect' of lithium polysulfides diffusing across to the anode and blocking Li^+ adsorption sites. To tackle both of these issues effectively, it is essential that both the active (sulfur) and conductive (MXene) materials are present in high concentrations throughout the structure, and that sulfur is able to expand and contract without damaging the electrode. To meet these criteria, macroporous MXene/S composite electrodes have been fabricated using alkalized $Ti_3C_2T_x$ nanoribbons (a-Ti_3C_2/S) [47] and crumpled N-$Ti_3C_2T_x$ (c-N-$Ti_3C_2T_x$/S) [42]. The high aspect ratio and flexibility of the nanoribbons enabled high sulfur loading (68 wt%) whilst maintaining complete entanglement of sulfur nanoparticles to provide short conduction paths and lots of free space to accommodate sulfur volume expansion and facilitate ionic diffusion [47]. In contrast, the N-$Ti_3C_2T_x$/S composite was fabricated *via* annealing with melted sulfur, creating a porous structure of S (74 wt%) around a MXene skeleton [42]. The choice of experiments presented in these publications makes it difficult to quantify the exact effect of the porous, nanoscopic architectures, but it is clear that both c-N-$Ti_3C_2T_x$ and a-$Ti_3C_2T_x$ morphologies were able to improve electrode cycling stability compared to 2D $Ti_3C_2T_x$, and therefore both morphologies are likely to be effective at reducing volume expansion and polysulfide shuttling.

By comparing the performances of $Na_{0.23}TiO_2$@Ti_3C_2 [110] and carbon nanotubes@Ti_3C_2 (CNTs@Ti_3C_2) [109] composites, it is possible to analyze the effect on Li-ion battery performance. Both of these composites contain aggregated groupings of small, 1D $Na_{0.23}TiO_2$ nanobelts and CNTs which facilitate highly reversible ion transport, and large, 2D MXene flakes which provide short conduction pathways for fast electron transport. Together these nanocomposites act as good examples to demonstrate the potential of their morphology to optimise the performance of high power electrodes, but there is again little evidence to quantify the level of enhancement directly attributable to the morpholgy. In studying the $Na_{0.23}TiO_2$@Ti_3C_2 composite, Huang *et al* used reaction time as a proxy to indirectly explore the effect of increasing the density of nanobelts on MXene sheets. They found that there was an optimal reaction time (100 h), which may be interpreted as an indication of

optimal porosity being attained, but inspection of the results presented (for example, the electrochemical impedance data) finds little evidence that increased $Na_{0.23}TiO_2$ nanobelt growth (and by extention, porosity) is aiding cation diffusion at all, which may mean that these pores are in a size regime much bigger than necessary to see a significant effect on Li^+ or Na^+ diffusion. To help elucidate the effect of the morphology of the CNTs@Ti_3C_2, the composite presented by Zheng *et al* [109] can be compared to CNT/Ti_3C_2 prepared by filtration of a mixed suspension [113]. Cyclic voltammetry of the two composites indicates that their energy storage mechanisms are similarly capacitive, although the CNTs@Ti_3C_2 is able to exhibit a small voltage plateau in the charge–discharge curves, which Zheng *et al* attributes to the presence of iron (used for *in situ* CNT synthesis). In spite of these similarities, the CNTs@Ti_3C_2 demonstrates significantly better cycling and rate performance. Since these improvements are not seen in other iron-containing MXene composites [114], this difference can, at least in part, be attributed to the morphology of the CNTs@Ti_3C_2 composite, which features a high specific surface area and strong physical connections between well-mixed composite components, which aids conductivity and prevents phase separation of composite components.

Initial computations attributed a theoretical capacity of 320 mAh g^{-1} to $Ti_3C_2Li_2$ [8], but it did not take long before a 'paper electrode' made by filtering delaminated flakes exceeded this (reaching 410 mAh g^{-1}), leading Mashtalir *et al* to hypothesize the reversible formation of a unique solid-electrolyte interphase (SEI) [105]. Recent work by Shen *et al* has shed some light on this issue by achieving facile Li metal plating on printed $Ti_3C_2T_x$ substrates. Not only has this work demonstrated that multiple layers of lithium are able to grow on MXenes when provided the space of a porous, printed structure (and hence also the extra inter-sheet space provided by $Ti_3C_2T_x$ exfoliation in the previous work), but also that the morphology of printed MXene arrays can homogenize Li^+ flux and electric field, which prevents the formation of destructive lithium dendrites during cycling. When paired with a $LiFePO_4$ cathode in a full-cell, fabricated anodes exhibited capacities of 111–150 mAh g^{-1} at rates of 1–30 C, with 99.4% capacity retention after 300 cycles at 1 C [92]. This type of Li anode production is in its infancy, and the actual capacities achieved were relatively low, but further optimization of this technique has the potential to create near-ideal anodes for Li-ion batteries.

The examples discussed in this section have demonstrated the importance and potential usefulness of considering the morphology of MXene-based battery electrodes at the nano, micro and macroscale. While effective flake exfoliation was enough to surpass the theoretically predicted performance of a simple $Ti_3C_2T_x$ Li-ion anode, the same cannot be said for the more complex systems of composite electrodes and other metal-ion batteries which require specially designed voids to improve cycling stability and rate performance without sacrificing internal conductivity and volumetric capacity. While these examples show clear performance improvements, the exact effects of 3D morphology are far from being quantified or understood, and it is necessary for the community to start investigating this directly in order to fully optimise all future MXene-based batteries.

6.2. Supercapacitors

The dominant pseudocapacitive storage mechanisms of MXenes make them promising candidates to be used as electrodes in supercapacitors as, they can achieve much higher energy densities than EDLCs, and higher power densities than batteries. However, despite their potential, to date the high theoretical capacitances estimated for different MXene phases [13, 116, 117] still far exceed the experimental results.

As discussed above, ion mobility and accessibility to the electrochemically active sites are significant concerns when trying to optimise electrochemical energy storage devices [13, 106, 118]. When Lukatskaya *et al* [13] investigated the discrepancy between the theoretical and experimental values of capacitance for MXene supercapacitors, they found that by producing an ultra-thin film (90 nm) of $Ti_3C_2T_x$, the ion transport limitations could be minimised and high performance (450 F g^{-1} at 10 mV s^{-1} for a 0.85 V potential window and rate performance of 63% at 10 V s^{-1}) achieved, approaching to the theoretical gravimetric capacitance of 615 C g^{-1} calculated for $Ti_3C_2O_{0.84(6)}(OH)_{0.06(2)}F_{0.25(8)}$. However, such a result is of limited applicability as it does not retain the performance when increasing the thickness of the film (e.g. 246 F g^{-1} at 2 mV s^{-1} for a 0.55 V potential window [17]). The impact of ion mobility and accessibility is also well illustrated by Li *et al* [118] for multilayered $Ti_3C_2T_x$ MXenes flakes by Trasatti method, showing that for higher scan rates (>20 mV s^{-1}) the capacitance is completely dominated by processes at the surface of the flakes (e.g. surface redox pseudocapacitance and EDLC) with no contribution from diffusion-limited processes (i.e. intercalation pseudocapacitance). In other words, at higher scan rates, the ions are not able to diffuse in between the 2D layers of highly stacked MXene flakes and reach redox active sites, hindering the electrodes rate performance [13, 55, 56]. Although there are a few techniques known to successfully exfoliate single 2D MXene sheets [11, 18, 24, 36] and thus enhance their surface availability, as discussed throughout the previous sections, careful control of the processing techniques is needed to prevent flake restacking. With that in mind, different

Table 3. Capacity properties of MXene-based 3D porous architectures as electrodes for supercapacitors.

References	Elctrode materials	Electrode morphology	Thickness, mass loading, density	Electrolyte, potential window	Grav., Vol. capacitances (areal capacitance) at scan rate	Rate performance
[13]	$Ti_3C_2T_x$	Vacuum-filtered ultra-thin film	90 nm	3 M H_2SO_4, −1.1 to −0.1 V (Hg/$HgSO_4$)	450 F g^{-1} at 10 mV s^{-1}	63% at 10 V s^{-1}
[17]	$Ti_3C_2T_x$	Rolled compact clay-film	5 μm	1 M H_2SO_4, −0.35 to 0.2 V (Ag/AgCl)	246 F g^{-1}, 910 F cm^{-3} at 2 mV s^{-1}	81% at 100 mV s^{-1}
			30 μm		182 F g^{-1}, 53 4 F cm^{-3} at 2 mV s^{-1}	63% at 100 mV s^{-1}
			75 μm		161 F g^{-1}, 35 5 F cm^{-3} at 2 mV s^{-1}	51% at 100 mV s^{-1}
[53]	$Ti_3C_2T_x$/carbon black	Film from slurry of freeze-dried porous particles	4 μm 1 mg cm^{-2}	1 M NaCl, −0.8 to −0.2 V (Ag/AgCl)	156 F g^{-1}, 41 0 F cm^{-3} at 5 mV s^{-1}	74% at 200 mV s^{-1}
				6 M KOH, −1.0 to −0.4 V (Ag/AgCl)	205 F g^{-1}, 53 5 F cm^{-3} at 5 mV s^{-1}	—
[13]	$Ti_3C_2T_x$	Hollow spheres macro-porous film	13 μm, 0.43 mg cm^{-2}, 0.35 g cm^{-3}	3 M H_2SO_4, −1.1 to −0.1 V (Hg/$HgSO_4$)	316 F g^{-1}, 11 0 F cm^{-3} (128 mF cm^{-2}) at 10 mV s^{-1}	91% at 1 V s^{-1} 67% at 10 V s^{-1}
			25 μm, 0.9 mg cm^{-2}, 0.35 g cm^{-3}		314 F g^{-1}, 11 0 F cm^{-3} (279 mF cm^{-2}) at 10 mV s^{-1}	84% at 1 V s^{-1} 38% at 10 V s^{-1}
			180 μm, 4.3 mg cm^{-2}, 0.35 g cm^{-3}		310 F g^{-1}, 108 F cm^{-3} (1333 mF cm^{-2}) at 10 mV s^{-1}	40% at 1 V s^{-1} 10% at 10 V s^{-1}
	Mo_2CT_x		30 μm, 0.6 mg cm^{-2}	3 M H_2SO_4, −0.8 to −0.16 V (Hg/$HgSO_4$)	160 F g^{-1} at 10 mV s^{-1}	79% at 1 V s^{-1} 38% at 10 V s^{-1}
[101]	$Ti_3C_2T_X$ /Bacterial Celullose	Macroporous Foam	5 mg cm^{-2}	3 M H_2SO_4, −0.7 to 0.1 V (Ag/AgCl)	416 F g^{-1} (2084 mF cm^{-2}) at 3 mA cm^{-2}	63% at 50 mA cm^{-2}
[55]	$Ti_3C_2T_x$	EDA-assisted freeze-dried aerogel	2 mg cm^{-2}	1 M KOH, −1.0 V to −0.4 (Ag/AgCl)	87 F g^{-1} (174 mF cm^{-2}) at 2 mV s^{-1}	77% at 10 mV s^{-1}
			15 mg cm^{-2}		68 F g^{-1} (1012 mF cm^{-2}) at 2 mV s^{-1}	47% at 10 mV s^{-1}
[119]	$Ti_3C_2T_x$	Freeze-cast aerogel	—	1 M Na_2SO_4, −0.8 to −0.2 V (Ag/AgCl)	67 F g^{-1}, 26 6 F cm^{-3} at 2 mV s^{-1}	—
	$Ti_3C_2T_x$/50 wt% NiO		—		77 F g^{-1}, 34 1 F cm^{-3} at 2 mV s^{-1}	—
[56]	$Ti_3C_2T_x$	Thiox/NH_3-assisted freeze-dried aerogel	0.14 mg cm^{-2}	3 M H_2SO_4, −0.6 to 0.2 (Ag/AgCl)	438 F g^{-1} at 10 mV s^{-1}	79% at 2 V s^{-1} 39% at 20 V s^{-1}
			1.82 mg cm^{-2}		427 F g^{-1} at 10 mV s^{-1}	77% at 100 mV s^{-1} 7% at 2 V s^{-1}
[54]	$Ti_3C_2T_X$	Ion-assisted freeze-dried aerogel	—	3 M H_2SO_4, −1.1 to −0.15 V (Hg/$HgSO_4$)	272 F g^{-1} at 2 mV s^{-1}	

Table 3. (Continued.)

References	Elctrode materials	Electrode morphology	Thickness, mass loading, density	Electrolyte, potential window	Grav., Vol. capacitances (areal capacitance) at scan rate	Rate performance
						92% at 100 mV s^{-1} 80% at 1 V s^{-1}
[72]	$Ti_3C_2T_x$	Unidirectional freeze-cast aerogel	10 mm, 0.011 g cm^{-3}	3 M H2SO4, −0.6 to −0.1 V (Ag/AgCl)	282 F g^{-1}, 3 F cm^{-3} at 10 mV s^{-1}	12% at 200 mV s^{-1}
		Rolled unidirectional freeze-cast aerogel	60 μm 1.030 g cm^{-3}	3 M H2SO4, −0.55 to −0.05 V (Ag/AgCl)	315 F g^{-1}, 32 3 F cm^{-3} at 10 mV s^{-1}	39% at 200 mV s^{-1}
			60 μm 0.434 g cm^{-3}		421 F g^{-1}, 18 3 F cm^{-3} at 10 mV s^{-1}	60% at 200 mV s^{-1}
[78]	$Ti_3C_2T_X$	Vertically Alligned Array ASSS	5 μm	PVA-H_3PO_4 0 to 0.6 V (CD), 0 to 0.7 V (CV)	485 F cm^{-3} at 0.5 A cm^{-3}	42% at 8 A cm^{-3}
			50 μm		354 F cm^{-3} at 0.5 A cm^{-3}	31% at 8 A cm^{-3}
[60]	$Ti_3C_2T_X$/rGO	Self-healing freeze-cast aerogel MSC	(aerogel density) 0.012 g cm^{-3}	PVA-H_2SO_4, 0 to 0.6 V	(34.6 mF cm^{-2}) at 1 mV s^{-1}	27% at 100 mV s^{-1}
[91]	N-$Ti_3C_2T_X$/AC/CNT/GO	Freeze-dried 3D printed composite	1 Layer 1.65 mm 21.67 mg cm^{-2}	PVA-H_2SO_4, 0 to 0.6 V	142 F g^{-1} at 3 mA cm^{-2} (3400 mF cm^{-2}) at 10 mV s^{-1}	47% at 12 mA cm^{-2}
			2 Layer 3.3 mm 42.25 mg cm^{-2}		120 F g^{-1} at 3 mA cm^{-2} (5200 mF cm^{-2}) at 10 mV s^{-1}	46% at 12 mA cm^{-2}
			3 Layer 4.95 mm 64.36 mg cm^{-2}		115 F g^{-1} at 12 mA cm^{-2} (8200 mF cm^{-2}) at 10 mV s^{-1}	39% at 12 mA cm^{-2}
[93]	$Ti_3C_2T_X$	Freeze-dried 3D printed MSC	1 Layer 8.5 mg cm^{-2}	PVA-H_2SO_4, 0 to 0.6 V	242.5 F g^{-1} (2070 mF cm^{-2}) at 1.7 mA cm^{-2}	94% at 4.3 mA cm^{-2} 45% at 42 mA cm^{-2}

processing techniques have been employed to produce 3D porous electrodes for supercapacitors, and are briefly listed on table 3.

The thiox/ammonia assisted, freeze-dried aerogel presented by Wang *et al* [56] showed an outstanding gravimetric capacitance of 438 F g^{-1} at 10 mV s^{-1} and good rate performance with a mass loading 0.14 mg cm^{-2}. However, when the mass loading was increased to 1.82 mg cm^{-2}, the gravimetric capacitance was maintained at 10 mV s^{-1}, but dropped to 7% of this value at 2 V s^{-1} due to the massive restacking of MXene flakes and reduced ion mobility. Lukatskaya *et al* [13] looked to improve the rate performance by assembling $Ti_3C_2T_x$ hollow spheres into macroporous films as discussed in section 4.2. A 13 μm thick macroporous film (c. a., 0.43 mg cm^{-2} mass loading) in 3 M H_2SO_4, showed a gravimetric capacitance of 310 F g^{-1} at 10 mV s^{-1} and exceptional rate performance, retaining 91% and 67% of the initial value at 1 V s^{-1} and 10 V s^{-1} respectively. By increasing these films thickness to 25 μm and 180 μm, higher areal capacitance was achieved, and the rate performance was still kept fairly high (84% and 40% at 1 V s^{-1} respectively). Unfortunately, while porous electrodes display higher gravimetric capacitance and rate performance compared to rolled, compact clay-films, the lower density of porous electrodes leads to a severe reduction in volumetric capacitance, making them less appropriate for miniaturised applications. On that note, to achieve high gravimetric and volumetric capacitances, and sustain these when performing at high rate, a higher control of the pore morphology is needed such that it facilitates ion mobility and accessibility without excessively decreasing the overall density of the electrode.

The optimisation of pore size—to balance ion mobility with volumetric density—was attempted by Bayram *et al* [72], who used a calendaring machine to compress $Ti_3C_2T_x$ aerogels to well-defined thicknesses. These aerogels had been produced by unidirectional freeze-casting, and thus were able to be compressed uniformly along the perpendicular direction to the aligned lammelae. Before compression, a 10 mm thick aerogel performed well in terms of its gravimetric capacitance (282 F g^{-1} at 10 mV s^{-1}); however, it had a very poor volumetric capacitance (3 F cm^{-3} at 10 mV s^{-1}) and rate performance (12% at 200 mV s^{-1}). When rolled and pressed to 60 μm thickness, ($\sim$1 g cm^{-3}) both the volumetric and gravimetric capacitance increased at 10 mV s^{-1} (323 F cm^{-3} and 315 F g^{-1}, respectively), with rate performance of 39% at 200 mV s^{-1}. Alternatively by pressing and rolling just a slice of the starting 10 mm aerogel, an electrode with the same 60 μm thickness, but lower density (0.434 g cm^{-3}) showed performance of 421 F g^{-1} and 183 F cm^{-3} at 10 mV s^{-1}, with rate performance of 60% at 200 mV s^{-1}. The improvement in capacitive performance of rolled MXene electrodes was attributed to their low charge-transfer resistance and the presence of small, micrometre scale (1 μm) accessible pores for optimum ion transport.

Attempting to take full advantage of an oriented porosity, hierarchical vertically aligned arrays of MXene (figure 9) were designed by Pan *et al* [78] (as discussed in section 4.3.2) and assembled into flexible, symmetric, all-solid-state supercapacitors (ASSS) in PVA-H_3PO_4 electrolyte. To improve its electrochemical performance, prior to the processing, the accordion-like MXene structures (prepared by concentrated HF etching) were immersed in 2 M KOH for 5 h, increasing their interlayer spacing. 3D structured electrodes showed an outstanding improvement in volumetric capacitance compared to spin-coated MXene slurry thin film electrodes and 72% of the high volumetric capacitance could be retained when increasing the electrode thickness from 5 to 50 μm.

Recently, works on 3D $Ti_3C_2T_x$ porous architectures have shown impressive areal capacitances. Porous $Ti_3C_2T_x$ assembled with bacterial cellulose (mass loading of 5 mg cm^{-2}) showed high gravimetric and areal capacitances (416 F g^{-1} and 2.084 mF cm^{-2}, respectively at 3 mA cm^{-2} with 5 mg cm^{-2} mass loading) and excellent mechanical strength, even at high deformation [101]. Meanwhile, some promising reports have started to pave the way for MXene based 3D printed electrodes [91, 93]. For example, freeze-dried extrusion printed $Ti_3C_2T_x$ electrodes (8.5 mg cm^{-2} mass loading) presented an areal capacitance of 2100 mF cm^{-2} with 242 F g^{-1} gravimetric capacitance at 1.7 mA cm^{-2} [93].

Another crucial factor in determining the capacitance of MXenes is their mix of terminations. Although the theoretical capacitance of bare pristine Ti_3C_2 is estimated to be 2131 F g^{-1} in^{-1} H-ion electrolyte, terminations are known to severely limit it (specially OH, S and F) [116]. Hu *et al* [120] showed that increasing the O/F ratio in $Ti_3C_2T_x$ enables it to provide a higher capacitance, estimating a specific capacitance of 1190 F g^{-1} for a MXene with formula $Ti_3C_2O_2$. Experimentally, the work of Li *et al* [118] demonstrated an increase in the specific capacitance of $Ti_3C_2T_x$ from 245 F g^{-1} to 517 F g^{-1} at 1 A g^{-1} by removing F and OH terminations and increasing the MXene inter-layer distance. In addition to those, the significant influence of the intercalated alkali-ions (e.g. Li^+, Na^+ and K^+) themselves on the pseudocapacitive contribution should be taken into account when analyzing the specific capacitance increase [121].

As can be seen in table 2, MXene aerogels were electrochemically tested with a few different electrolytes and electrode parameters achieving a wide range of performance values [13, 55, 56, 119]. This variety of test parameters and the lack of some fundamental information of the electrodes make it hard to compare samples' performances. The performance of supercapacitor electrodes strongly relies on the type of electrolyte, electrode/

electrolyte interactions, solvated ion size, and the accessibility of ions to the full interior of electrode. Aqueous electrolyte, for example, is usually the best choice regarding safety, toxicity and cost, but has a limited potential window determined by the thermodynamic limit of water (1.23 V) [122]. Usually H_2SO_4 electrolyte is used for $Ti_3C_2T_x$ MXene (instead of Li_2SO_4, Na_2SO_4, and K_2SO_4), since H^+ ions have smaller radii and higher ionic mobility, promoting faster intercalation into the MXene layers and faster surface redox reactions [118]. Higher molar concentration of H_2SO_4 can slightly increase specific capacitance and the rate performance due to higher ionic conductivity [13]. Generally MXene-based electrodes have good cycle stability, retaining more than 90% their initial capacitance after thousands of cycles, but interestingly $Ti_3C_2T_x$ aerogels tested in Na-based electrolytes, such as NaCl and Na_2SO_4, actually show an increase of capacitance with cycling, which is arguably due to deeper Na^+ intercalation over time [53, 119]. Moreover, soaking the electrodes in the electrolytes for an extended period of time to form a hydrogel before measurements is known to enhance measured electrochemical performance, as it allows time for the electrolyte species to reach the active sites [13].

Despite its promising values of capacitance, MXenes have consistently shown small potential windows, usually narrower than 1 V. Although not extensively investigated for MXenes yet, organic or ionic electrolytes are interesting alternatives to provide extended potential windows up to 3 V, which is essential to drastically improve the energy density [123–125]. Nevertheless, safety issues, toxicity, electrolyte decomposition, temperature/humidity sensitivity and high cost make these electrolytes less desirable for most applications [122]. An alternative strategy to increase the potential window would be designing an aqueous asymmetric supercapacitor [126–128]. It has been shown that MXene-based aqueous, asymmetric supercapacitors can be operated up to 2.2 V, making MXenes a promising alternative to carbon-based anodes [128].

As discussed through this and previous sections, several parameters can influence the measured electrochemical performance of the materials, and these must be systematically provided and discussed for proper research regarding the materials' macro and microstructures impact on energy storage devices. Some parameters which are frequently overlooked or not provided, include sample dimensions, density, mass loading, soaking time in electrolyte prior to measurement, and performance at higher scan rates.

7. Challenges and future outlook

The last few years have seen increasing interest in the processing of 3D architectures with controlled microstructures using 2D materials as building blocks. Most of the reported progress has been on graphene-based materials for energy and environmental applications. MXene-based materials have shown rapid evolution due to the experience already acquired from the processing and characterization methods of its 2D predecessor. The advances in 3D printing technologies are particularly exciting for the processing of 2D materials and despite few reports to date with MXene-based inks, results are promising. However, before the potential of 3D MXenes can be fully realized on an industrial scale, there are challenges which must be overcome in their synthesis, processing and application:

- *Quality and reproducibility*: MXenes' versatile composition introduces further complexity; even small changes in synthesis conditions change the degree of etching, intercalation and exfoliation, and the surface terminations of flakes. These impact their physical properties, stability and processability. Therefore, a deeper understanding of the synthesis is required to gain better control, and ensure reproducibility in the number of stacked sheets with known interlayer spacing and flake size.
- *Cost and sustainability*: While chemical reliability and quality are being improved, synthesis remains very expensive (even more so when considering the cost of the MAX phase precursor) and far from eco-friendly; very few works have proposed suitable fluorine-free syntheses.
- *Structure control*: As for all functional 3D architectures, properties such as pore-size and morphology, hydrophilicity, and conductivity are very important for their performance, so further investigation into high-precision processing is needed to determine the influence of each parameter in each application. By controlling pore size and morphology, for example, ion mobility and accessibility could be optimized for electrochemical energy storage. Aligned pores can facilitate ion transport, enabling enhanced and nearly thickness-independent electrochemical behavior. Besides electrochemical storage, the precise control of directional ion transport is critical to other energy fields like photovoltaics, fuel cells and catalysis.
- *Flake size*: MXenes lateral flake size is still limited to less than 10 μm due to the available syntheses and intercalation methods; limiting their potential for several applications. Bottom-up synthesis, such as chemical vapor deposition of MXenes, might overcome this challenge, but no successful methods to produce monolayer flakes have been reported to date.

- *Comparable reports*: As has been discussed, just a few 3D processing techniques have been applied to MXenes so far, such as freeze casting and making frameworks from previously formed hierarchical particles, but even those lack sufficient reports and critical scrutiny. Although understandable, being still in an exploration phase, studies lack a degree of optimization and standardization in their characterization methods, making it difficult to systematically review the processing-structure-property relations.
- *Full-cell tests*: Most reported 3D porous structures for electrochemical energy storage were tested in half-cell systems. Despite being a practical method for evaluating the potential of such materials, for practical applications, the actual power, rate and volumetric capabilities strongly depend on the full-cell composition and designs, which are yet to be explored.
- *Other MXenes, beyond* $Ti_3C_2T_x$: As a diverse family of compounds, MXenes have the potential to be specifically tuned for each application with far more versatility than other 2D materials. The most commonly studied MXene, $Ti_3C_2T_x$, already presents outstanding properties not only for energy storage applications, but also electromagnetic shielding, environmental cleaning, catalysis and sensors. Several other MXenes, such as Ti_2CT_x and V_2CT_x, were reported and theorized to have arguably better properties than $Ti_3C_2T_x$ for specific applications; however the progress in the research of these alternative compositions presents specific challenges of its own and still need much more investigation.

This review has discussed a number of techniques that enable the assembly of 2D MXenes into 3D architectures, highlighting the importance of this field in energy applications and limitations for progress. Ultimately, if devices in future energy technologies are to significantly benefit from the properties of 2D materials such as MXenes, engineers and scientists must develop the capabilities to design and fabricate products with structural and compositional control at multiple length scales. Research should be directed into the development of new, multi-scale manufacturing approaches that can incorporate 2D materials such as MXenes, supported by advanced characterizations, simulation and modeling (from processing to properties) in order to enable the realization of optimized structure-property relations in future products and devices for energy storage and beyond.

Acknowledgments

This study was partially financed by the Coordenação de Aperfeiçoamento de Pessoal de Nível Superior, Brasil (CAPES). The authors would also like to acknowledge the support of: Graphene NOWNANO CDT, funded through EPSRC grant (EP/L01548X/1), United Kingdom; Heilongjiang Huasheng Graphite Co. Ltd, People's Republic of China; the Newton-Katip Celebi Fund provided by The Scientific and Technological Research Council of Turkey (TUBITAK), Turkey; and British Council, United Kingdom.

ORCID iDs

G Tontini https://orcid.org/0000-0002-2453-6358
M Greaves https://orcid.org/0000-0002-0924-8083
S Ghosh https://orcid.org/0000-0002-5189-7853
V Bayram https://orcid.org/0000-0001-9781-4980
S Barg https://orcid.org/0000-0002-0723-7081

References

[1] Novoselov K S, Geim A K, Morozov S V, Jiang D, Zhang Y, Dubonos S V, Grigorieva I V and Firsov A A 2004 Electric field in atomically thin carbon films *Science* **306** 666–9
[2] Wu Y, Zhu J and Huang L 2019 A review of three-dimensional graphene-based materials: synthesis and applications to energy conversion/storage and environment *Carbon* **143** 610–40
[3] Cong H P, Chen J F and Yu S H 2014 Graphene-based macroscopic assemblies and architectures: an emerging material system *Chem. Soc. Rev.* **43** 7295–325
[4] Qiu B, Xing M and Zhang J 2018 Recent advances in three-dimensional graphene based materials for catalysis applications *Chem. Soc. Rev.* **47** 2165–216
[5] Wang H F, Tang C and Zhang Q 2019 A review of graphene-based 3D van der Waals hybrids and their energy applications *Nano Today* **25** 27–37
[6] Pacilé D, Meyer J C, Girit Ç Ö and Zettl A 2008 The two-dimensional phase of boron nitride: Few-atomic-layer sheets and suspended membranes *Appl. Phys. Lett.* **92** 133107
[7] Ma R and Sasaki T 2010 Nanosheets of oxides and hydroxides: ultimate 2D charge-bearing functional crystallites *Adv. Mater.* **22** 5082–104

[8] Naguib M, Kurtoglu M, Presser V, Lu J, Niu J, Heon M, Hultman L, Gogotsi Y and Barsoum M W 2011 Two-dimensional nanocrystals produced by exfoliation of Ti 3AlC 2 *Adv. Mater.* **23** 4248–53

[9] Anasori B and Gogotsi Y 2019 2D Metal Carbides and Nitrides (MXenes) (Cham: Springer) (https://doi.org/10.1007/978-3-030-19026-2)

[10] Verger L, Xu C, Natu V, Cheng H-M, Ren W and Barsoum M W 2019 Overview of the synthesis of MXenes and other ultrathin 2D transition metal carbides and nitrides *Curr. Opin. Solid State Mater. Sci.* **23** 149–63

[11] Anasori B, Lukatskaya M R and Gogotsi Y 2017 2D metal carbides and nitrides (MXenes) for energy storage *Nat. Rev. Mater.* **2** 16098

[12] Chaudhari N K, Jin H, Kim B, San Baek D, Joo S H and Lee K 2017 MXene: an emerging two-dimensional material for future energy conversion and storage applications *J. Mater. Chem.* A **5** 24564–79

[13] Lukatskaya M R *et al* 2017 Ultra-high-rate pseudocapacitive energy storage in two-dimensional transition metal carbides *Nat. Energy* **6** 1–6

[14] Li G, Kushnir K, Dong Y, Chertopalov S, Rao A M, Mochalin V N, Podila R and Titova L V 2018 Equilibrium and non-equilibrium free carrier dynamics in 2D $Ti_3C_2T_x$ MXenes: THz spectroscopy study *2D Mater.* **5** 035043

[15] Pang J, Mendes R G, Bachmatiuk A, Zhao L, Ta H Q, Gemming T, Liu H, Liu Z and Rummeli M H 2019 Applications of 2D MXenes in energy conversion and storage systems *Chem. Soc. Rev.* **48** 72–133

[16] Cui J, Peng Q, Zhou J and Sun Z 2019 Strain-tunable electronic structures and optical properties of semiconducting MXenes *Nanotechnology* **30** 345205

[17] Ghidiu M, Lukatskaya M R, Zhao M-Q, Gogotsi Y and Barsoum M W 2014 Conductive two-dimensional titanium carbide 'clay' with high volumetric capacitance *Nature* **516** 78–81

[18] Liu Y T, Zhu X D and Pan L 2018 Hybrid architectures based on 2D MXenes and low-dimensional inorganic nanostructures: methods, synergies, and energy-related applications *Small* **14** 1–22

[19] Liu Z *et al* 2019 Three-dimensional ordered porous electrode materials for electrochemical energy storage *NPG Asia Mater.* **11** 12

[20] Liu R, Duay J and Lee S B 2011 Heterogeneous nanostructured electrode materials for electrochemical energy storage *Chem. Commun.* **47** 1384–404

[21] Lukatskaya M R, Dunn B and Gogotsi Y 2016 Multidimensional materials and device architectures for future hybrid energy storage *Nat. Commun.* **7** 12647

[22] Ghodbane O, Pascal J L and Favier F 2009 Microstructural effects on charge-storage properties in MnO_2-based electrochemical supercapacitors *ACS Appl. Mater. Interfaces* **1** 1130–9

[23] Wang Q, Yan J and Fan Z 2016 Carbon materials for high volumetric performance supercapacitors: design, progress, challenges and opportunities *Energy Environ. Sci.* **9** 729–62

[24] Alhabeb M, Maleski K, Anasori B, Lelyukh P, Clark L, Sin S and Gogotsi Y 2017 Guidelines for synthesis and processing of two-dimensional titanium carbide (Ti 3 C 2 T x MXene) *Chem. Mater.* **29** 7633–44

[25] Zhu J *et al* 2017 Recent advance in MXenes: a promising 2D material for catalysis, sensor and chemical adsorption *Coord. Chem. Rev.* **352** 306–27

[26] Zhang Y, Wang L, Zhang N and Zhou Z 2018 Adsorptive environmental applications of MXene nanomaterials: a review *RSC Adv.* **8** 19895–905

[27] Karlsson L H, Birch J, Halim J, Barsoum M W and Persson P O Å 2015 Atomically resolved structural and chemical investigation of single MXene sheets *Nano Lett.* **15** 4955–60

[28] Hope M A, Forse A C, Griffith K J, Lukatskaya M R, Ghidiu M, Gogotsi Y and Grey C P 2016 NMR reveals the surface functionalisation of Ti3C2 MXene *Phys. Chem. Chem. Phys.* **18** 5099–102

[29] Pang S Y, Wong Y T, Yuan S, Liu Y, Tsang M K, Yang Z, Huang H, Wong W T and Hao J 2019 Universal strategy for HF-free facile and rapid synthesis of two-dimensional MXenes as multifunctional energy materials *J. Am. Chem. Soc.* **141** 9610–6

[30] Sun W, Shah S A, Chen Y, Tan Z, Gao H, Habib T, Radovic M and Green M J 2017 Electrochemical etching of Ti_2AlC to Ti_2CT:X (MXene) in low-concentration hydrochloric acid solution *J. Mater. Chem.* A **5** 21663–8

[31] Yang S, Zhang P, Wang F, Ricciardulli A G, Lohe M R, Blom P W M and Feng X 2018 Fluoride-free synthesis of two-dimensional titanium carbide (MXene) using a binary aqueous system *Angew. Chem.—Int. Ed.* **57** 15491–5

[32] Li T *et al* 2019 Fluorine-free $Ti_3C_2T_x$ (T = O, OH) nanosheets (~50 to 100 nm) for nitrogen fixation under ambient conditions *J. Mater. Chem.* A **7** 14462–5

[33] Li T *et al* 2018 Fluorine-free synthesis of high-purity $Ti_3C_2T_x$ (T = OH, O) via alkali treatment *Angew. Chem.—Int. Ed.* **57** 6115–9

[34] Li M *et al* 2019 Element replacement approach by reaction with lewis acidic molten salts to synthesize nanolaminated MAX phases and MXenes *J. Am. Chem. Soc.* **141** 4730–7

[35] Zhang B, Zhu J, Shi P, Wu W and Wang F 2019 Fluoride-free synthesis and microstructure evolution of novel two-dimensional $Ti_3C_2(OH)_2$ nanoribbons as high-performance anode materials for lithium-ion batteries *Ceram. Int.* **45** 8395–405

[36] Luo J *et al* 2017 Pillared structure design of MXene with ultralarge interlayer spacing for high-performance lithium-ion capacitors *ACS Nano* **11** 2459–69

[37] Urbankowski P, Anasori B, Makaryan T, Er D, Kota S, Walsh P L, Zhao M, Shenoy V B, Barsoum M W and Gogotsi Y 2016 Synthesis of two-dimensional titanium nitride Ti_4N_3(MXene) *Nanoscale* **8** 11385–91

[38] Urbankowski P, Anasori B, Hantanasirisakul K, Yang L, Zhang L, Haines B, May S J, Billinge S J L and Gogotsi Y 2017 2D molybdenum and vanadium nitrides synthesized by ammoniation of 2D transition metal carbides (MXenes) *Nanoscale* **9** 17722–30

[39] Verger L, Natu V, Carey M and Barsoum M W 2019 MXenes: an introduction of their synthesis, select properties, and applications *Trends Chem.* **1** 656–69

[40] Zhao M Q, Xie X, Ren C E, Makaryan T, Anasori B, Wang G and Gogotsi Y 2017 Hollow MXene spheres and 3D macroporous MXene frameworks for Na-Ion storage *Adv. Mater.* **29** 1702410

[41] Shah S A, Habib T, Gao H, Gao P, Sun W, Green M J and Radovic M 2017 Template-free 3D titanium carbide ($Ti_3C_2T_x$) MXene particles crumpled by capillary forces *Chem. Commun.* **53** 400–3

[42] Bao W, Liu L, Wang C, Choi S, Wang D and Wang G 2018 Facile synthesis of crumpled nitrogen-doped MXene nanosheets as a new sulfur host for lithium-sulfur batteries *Adv. Energy Mater.* **8** 1702485

[43] Zhao D, Clites M, Ying G, Kota S, Wang J, Natu V, Wang X, Pomerantseva E, Cao M and Barsoum M W 2018 Alkali-induced crumpling of $Ti_3C_2T_x$ (MXene) to form 3D porous networks for sodium ion storage *Chem. Commun.* **54** 4533–6

[44] Natu V, Clites M, Pomerantseva E and Barsoum M W 2018 Mesoporous MXene powders synthesized by acid induced crumpling and their use as Na-ion battery anodes *Mater. Res. Lett.* **6** 230–5

[45] Xiu L, Wang Z, Yu M, Wu X and Qiu J 2018 Aggregation-resistant 3D MXene-based architecture as efficient bifunctional electrocatalyst for overall water splitting *ACS Nano* **12** 8017–28

[46] Lian P, Dong Y, Wu Z S, Zheng S, Wang S, Sun C, Qin J, Shi X and Bao X 2017 Alkalized Ti_3C_2 MXene nanoribbons with expanded interlayer spacing for high-capacity sodium and potassium ion batteries *Nano Energy* **40** 1–8
[47] Dong Y, Zheng S, Qin J, Zhao X, Shi H, Wang X, Chen J and Wu Z S 2018 All-MXene-based integrated electrode constructed by Ti_3C_2 nanoribbon framework host and nanosheet interlayer for high-energy-density Li-S batteries *ACS Nano* **12** 2381–8
[48] Wu X, Wang Z, Yu M, Xiu L and Qiu J 2017 Stabilizing the MXenes by carbon nanoplating for developing hierarchical nanohybrids with efficient lithium storage and hydrogen evolution capability *Adv. Mater.* **29** 1607017
[49] Wu F, Jiang Y, Ye Z, Huang Y, Wang Z, Li S, Mei Y, Xie M, Li L and Chen R 2019 A 3D flower-like VO_2/MXene hybrid architecture with superior anode performance for sodium ion batteries *J. Mater. Chem.* A **7** 1315–22
[50] Wang Y, Dou H, Wang J, Ding B, Xu Y, Chang Z and Hao X 2016 Three-dimensional porous MXene/layered double hydroxide composite for high performance supercapacitors *J. Power Sources* **327** 221–8
[51] Liu J, Zhang H B, Sun R, Liu Y, Liu Z, Zhou A and Yu Z Z 2017 Hydrophobic, flexible, and lightweight MXene foams for high-performance electromagnetic-interference shielding *Adv. Mater.* **29** 1702367
[52] Ma Z, Zhou X, Deng W, Lei D and Liu Z 2018 3D porous MXene (Ti_3C_2)/reduced graphene oxide hybrid films for advanced lithium storage *ACS Appl. Mater. Interfaces* **10** 3634–43
[53] Bao W, Tang X, Guo X, Choi S, Wang C, Gogotsi Y and Wang G 2018 Porous cryo-dried MXene for efficient capacitive deionization *Joule* **2** 778–87
[54] Deng Y *et al* 2019 Fast gelation of $Ti_3C_2T_x$ MXene initiated by metal ions *Adv. Mater.* **31** 1902432
[55] Li L, Zhang M, Zhang X and Zhang Z 2017 New Ti_3C_2 aerogel as promising negative electrode materials for asymmetric supercapacitors *J. Power Sources* **364** 234–41
[56] Wang X, Fu Q, Wen J, Ma X, Zhu C, Zhang X and Qi D 2018 3D Ti_3C_2T :X aerogels with enhanced surface area for high performance supercapacitors *Nanoscale* **10** 20828–35
[57] Liu J, Zhang H B, Xie X, Yang R, Liu Z, Liu Y and Yu Z Z 2018 Multifunctional, superelastic, and lightweight mxene/polyimide aerogels *Small* **14** 1–10
[58] Wang C, Chen X, Wang B, Huang M, Wang B, Jiang Y and Ruoff R S 2018 Freeze-casting produces a graphene oxide aerogel with a radial and centrosymmetric structure *ACS Nano* **12** 5816–25
[59] Tong Y, He M, Zhou Y, Nie S, Zhong X, Fan L, Huang T, Liao Q and Wang Y 2018 Three-dimensional hierarchical architecture of the TiO_2/$Ti_3C_2T_x$/RGO ternary composite aerogel for enhanced electromagnetic wave absorption *ACS Sustain. Chem. Eng.* **6** 8212–22
[60] Yue Y *et al* 2018 Highly self-healable 3D microsupercapacitor with MXene-graphene composite aerogel *ACS Nano* **12** 4224–32
[61] Zhao S, Zhang H B, Luo J Q, Wang Q W, Xu B, Hong S and Yu Z Z 2018 Highly Electrically conductive three-dimensional $Ti_3C_2T_x$ MXene/reduced graphene oxide hybrid aerogels with excellent electromagnetic interference shielding performances *ACS Nano* **12** 11193–202
[62] Ma Y *et al* 2018 3D synergistical MXene/reduced graphene oxide aerogel for a piezoresistive sensor *ACS Nano* **12** 3209–16
[63] Shang T, Lin Z, Qi C, Liu X, Li P, Tao Y, Wu Z, Li D, Simon P and Yang Q 2019 3D Macroscopic architectures from self-assembled MXene hydrogels *Adv. Funct. Mater.* **29** 1903960
[64] Scotti K L and Dunand D C 2018 Freeze casting—a review of processing, microstructure and properties via the open data repository, FreezeCasting.net *Prog. Mater Sci.* **94** 243–305
[65] Nelson I and Naleway S E 2019 Intrinsic and extrinsic control of freeze casting *J. Mater. Res. Technol.* **8** 2372–85
[66] Deville S, Saiz E, Nalla R K and Tomsia A P 2006 Freezing as a path to build complex composites *Science* **311** 515–8
[67] Qiu L, Liu J Z, Chang S L Y, Wu Y and Li D 2012 Biomimetic superelastic graphene-based cellular monoliths *Nat. Commun.* **3** 1–7
[68] Barg S, Perez F M, Ni N, Do Vale Pereira P, Maher R C, Garcia-Tuñon E, Eslava S, Agnoli S, Mattevi C and Saiz E 2014 Mesoscale assembly of chemically modified graphene into complex cellular networks *Nat. Commun.* **5** 4328
[69] Shao Y, El-Kady M F, Lin C W, Zhu G, Marsh K L, Hwang J Y, Zhang Q, Li Y, Wang H and Kaner R B 2016 3D freeze-casting of cellular graphene films for ultrahigh-power-density supercapacitors *Adv. Mater.* **28** 6719–26
[70] Han M *et al* 2019 Anisotropic MXene aerogels with a mechanically tunable ratio of electromagnetic wave reflection to absorption *Adv. Opt. Mater.* **7** 1900267
[71] Bian R, He G, Zhi W, Xiang S, Wang T and Cai D 2019 Ultralight MXene-based aerogels with high electromagnetic interference shielding performance *J. Mater. Chem.* C **7** 474–8
[72] Bayram V, Ghidiu M, Lindley M, Fairclough S, Haigh S J, Barsoum M W, Kinloch I A and Barg S 2020 MXene tuneable lamellae architectures for supercapacitor electrodes *ACS Appl. Energy Mater.* **3** 1 411–22
[73] Bai H, Chen Y, Delattre B, Tomsia A P and Ritchie R O 2015 Bioinspired large-scale aligned porous materials assembled with dual temperature gradients *Sci. Adv.* **1** e1500849
[74] Deville S 2017 *Freezing Colloids: Observations, Principles, Control, and Use* (Cham: Springer) (https://doi.org/10.1007/978-3-319-50515-2)
[75] Hu M, Li Z, Zhang H, Hu T, Zhang C, Wu Z and Wang X 2015 Self-assembled $Ti_3C_2T_x$ MXene film with high gravimetric capacitance *Chem. Commun.* **51** 13531–3
[76] Bian R, Lin R, Wang G, Lu G, Zhi W, Xiang S, Wang T, Clegg P S, Cai D and Huang W 2018 3D assembly of Ti_3C_2-MXene directed by water/oil interfaces *Nanoscale* **10** 3621–5
[77] Yuan W, Yang K, Peng H, Li F and Yin F 2018 A flexible VOCs sensor based on a 3D Mxene framework with a high sensing performance *J. Mater. Chem.* A **6** 18116–24
[78] Pan Q, Duan C, Liu H, Li M, Zhao Z, Zhao D, Duan Y, Chen Y and Wang Y 2019 Hierarchical vertically aligned titanium carbide (MXene) array for flexible all-solid-state supercapacitor with high volumetric capacitance *ACS Appl. Energy Mater.* **2** 6834–40
[79] Xu C, Kang N, Wang L, Cheng H-M, Ma X-L, Liu Z, Chen L, Ren W and Guo J 2015 Large-area high-quality 2D ultrathin Mo2C superconducting crystals *Nat. Mater.* **14** 1135–41
[80] Drieschner S, Weber M, Wohlketzetter J, Vieten J, Makrygiannis E, Blaschke B M, Morandi V, Colombo L, Bonaccorso F and Garrido J A 2016 High surface area graphene foams by chemical vapor deposition *2D Mater.* **3** 045013
[81] Lewis J A 2006 Direct ink writing of 3D functional materials *Adv. Funct. Mater.* **16** 2193–204
[82] Garcia-Tunon E, Barg S, Franco J, Bell R, Eslava S, D'Elia E, Maher R C, Guitian F and Saiz E 2015 Printing in three dimensions with graphene *Adv. Mater.* **27** 1688–93
[83] Guo H, Lv R and Bai S 2019 Recent advances on 3D printing graphene-based composites *Nano Mater. Sci.* **1** 101–15
[84] Wang J, Liu Y, Fan Z, Wang W, Wang B and Guo Z 2019 Ink-based 3D printing technologies for graphene-based materials: a review *Adv. Compos. Hybrid Mater.* **2** 1–33
[85] Akuzum B, Maleski K, Anasori B, Lelyukh P, Alvarez N J, Kumbur E C and Gogotsi Y 2018 Rheological characteristics of 2D titanium carbide (MXene) dispersions: a guide for processing MXenes *ACS Nano* **12** 2685–94

[86] Naficy S, Jalili R, Aboutalebi S H, Gorkin R A, Konstantinov K, Innis P C, Spinks G M, Poulin P and Wallace G G 2014 Graphene oxide dispersions: tuning rheology to enable fabrication *Mater. Horizons* **1** 326–31

[87] Natu V, Sokol M, Verger L and Barsoum M W 2018 Effect of edge charges on stability and aggregation of $Ti_3C_2T_z$ MXene colloidal suspensions *J. Phys. Chem.* C **122** 27745–53

[88] Quain E, Mathis T S, Kurra N, Maleski K, Van Aken K L, Alhabeb M, Alshareef H N and Gogotsi Y 2019 Direct writing of additive-free MXene-in-water ink for electronics and energy storage *Adv. Mater. Technol.* **4** 1800256

[89] Zhang C J, Kremer M P, Seral-Ascaso A, Park S H, McEvoy N, Anasori B, Gogotsi Y and Nicolosi V 2018 Stamping of flexible, coplanar micro-supercapacitors using MXene inks *Adv. Funct. Mater.* **28** 1705506

[90] Zhang C (J) *et al* 2019 Additive-free MXene inks and direct printing of micro-supercapacitors *Nat. Commun.* **10** 1795

[91] Yu L, Fan Z, Shao Y, Tian Z, Sun J and Liu Z 2019 Versatile N-doped MXene ink for printed electrochemical energy storage application *Adv. Energy Mater.* 1901839

[92] Shen K, Li B and Yang S 2020 3D printing dendrite-free lithium anodes based on the nucleated MXene arrays *Energy Storage Mater.* **24** 670–5

[93] Yang W *et al* 2019 3D Printing of Freestanding MXene Architectures for Current-Collector-Free Supercapacitors *Adv. Mater.* **31** 1902725

[94] Jiang Y, Xu Z, Huang T, Liu Y, Guo F, Xi J, Gao W and Gao C 2018 Direct 3D printing of ultralight graphene oxide aerogel microlattices *Adv. Funct. Mater.* **28** 1–8

[95] Julbe A and Ramsay J D F 1996 Chapter 4 Methods for the characterisation of porous structure in membrane materials *Membrane Sci. Tech.* **4** 67–118

[96] Haugen H J and Bertoldi S 2017 2 - Characterization of morphology—3D and porous structure *Characterization of Poly. Bio.* 21–53

[97] Rouquerol J, Avnir D, Fairbridge C W, Everett D H, Haynes J M, Pernicone N, Ramsay J D F, Sing K S W and Unger K K 1994 Recommendations for the characterization of porous solids (Technical Report) *Pure Appl. Chem.* **66** 1739–58

[98] Du Plessis A, Yadroitsev I, Yadroitsava I and Le Roux S G 2018 X-ray microcomputed tomography in additive manufacturing: a review of the current technology and applications *3D Print. Addit. Manuf.* **5** 227–47

[99] Rouquerol J, Llewellyn P and Rouquerol F 2007 Is the bet equation applicable to microporous adsorbents? *Stud.Surface Sci. Cat.* **160** 49–56

[100] ISO 9277:2010 2010 *Determination of the Specific Surface Area of Solids by Gas Adsorption—BET Method* (International Organisation for Standardization)

[101] Wang Y, Wang X, Li X, Bai Y, Xiao H, Liu Y, Liu R and Yuan G 2019 Engineering 3D ion transport channels for flexible MXene films with superior capacitive performance *Adv. Funct. Mater.* **29** 1–10

[102] Sun H, Zhu J, Baumann D, Peng L, Xu Y, Shakir I, Huang Y and Duan X 2019 Hierarchical 3D electrodes for electrochemical energy storage *Nat. Rev. Mater.* **4** 45–60

[103] Werner J G, Rodríguez-Calero G G, Abruña H D and Wiesner U 2018 Block copolymer derived 3D interpenetrating multifunctional gyroidal nanohybrids for electrical energy storage *Energy Environ. Sci.* **11** 1261–70

[104] Xie Y, Naguib M, Mochalin V N, Barsoum M W, Gogotsi Y, Yu X, Nam K-W, Yang X-Q, Kolesnikov A I and Kent P R C 2014 Role of surface structure on Li-ion energy storage capacity of two-dimensional transition-metal carbides *J. Am. Chem. Soc.* **136** 6385–94

[105] Mashtalir O, Naguib M, Mochalin V N, Dall'Agnese Y, Heon M, Barsoum M W and Gogotsi Y 2013 Intercalation and delamination of layered carbides and carbonitrides *Nat. Commun.* **4** 1716

[106] Xia Y, Mathis T S, Zhao M Q, Anasori B, Dang A, Zhou Z, Cho H, Gogotsi Y and Yang S 2018 Thickness-independent capacitance of vertically aligned liquid-crystalline MXenes *Nature* **557** 409–12

[107] Greaves M, Barg S and Bissett M A 2020 A review of MXene-based anodes for metal-ion batteries *Batteries & Supercaps* **3** 1–23

[108] Zhao D, Clites M, Ying G, Kota S, Wang J, Natu V, Wang X, Cao M, Pomerantseva E and Barsoum M W 2018 Alkali-induced crumpling of Ti3C2Tx (MXene) to form 3D porous networks for sodium ion storage *Chem. Commun.* **54** 2–5

[109] Zheng W, Zhang P, Chen J, Tian W B, Zhang Y M and Sun Z M 2018 *In situ* synthesis of CNTs@Ti_3C_2 hybrid structures by microwave irradiation for high-performance anodes in lithium ion batteries *J. Mater. Chem.* A **6** 3543–51

[110] Huang J, Meng R, Zu L, Wang Z, Feng N, Yang Z, Yu Y and Yang J 2018 Sandwich-like $Na_{0.23}TiO_2$ nanobelt/Ti_3C_2 MXene composites from a scalable *in situ* transformation reaction for long-life high-rate lithium/sodium-ion batteries *Nano Energy* **46** 20–8

[111] Zheng W, Zhang P G, Chen J, Tian W B, Zhang Y M and Sun Z M 2019 Microwave-assisted synthesis of three-dimensional MXene derived metal oxide/carbon nanotube/iron hybrids for enhanced lithium-ions storage *J. Electroanal. Chem.* **835** 205–11

[112] Zhao M-Q, Torelli M, Ren C E, Ghidiu M, Ling Z, Anasori B, Barsoum M W and Gogotsi Y 2016 2D titanium carbide and transition metal oxides hybrid electrodes for Li-ion storage *Nano Energy* **30** 603–13

[113] Liu Y, Wang W, Ying Y, Wang Y and Peng X 2015 Binder-free layered Ti_3C_2/CNTs nanocomposite anodes with enhanced capacity and long-cycle life for lithium-ion batteries *Dalt. Trans.* **44** 7123–6

[114] Wang Y, Li Y, Qiu Z, Wu X, Zhou P, Zhou T, Zhao J, Miao Z, Zhou J and Zhuo S 2018 Fe_3O_4@Ti_3C_2 MXene hybrid with ultrahigh volumetric capacity as anode material for lithium-ion battery *J. Mater. Chem.* A **6** 11189–97

[115] Yang C, Liu Y, Sun X, Zhang Y, Hou L, Zhang Q and Yuan C 2018 *In-situ* construction of hierarchical accordion-like TiO_2/Ti_3C_2 nanohybrid as anode material for lithium and sodium ion batteries *Electrochim. Acta* **271** 165–72

[116] Wang L, Wang J, Zhang Z, Wang L, Wang W, Liu J, Hong Z, Cho K and Wang W 2019 Origin of theoretical pseudocapacitance of two-dimensional supercapacitor electrodes $Ti_3C_2T_2$ (T = bare, O, S) *J. Mater. Chem. A* **7** 16231–8

[117] Xin Y and Yu Y X 2017 Possibility of bare and functionalized niobium carbide MXenes for electrode materials of supercapacitors and field emitters *Mater. Des.* **130** 512–20

[118] Li J, Yuan X, Lin C, Yang Y, Xu L, Du X, Xie J, Lin J and Sun J 2017 Achieving high pseudocapacitance of 2D titanium carbide (MXene) by cation intercalation and surface modification *Adv. Energy Mater.* **7** 1602725

[119] Zhang K, Ying G, Liu L, Ma F, Su L, Zhang C, Wu D, Wang X and Zhou Y 2019 Three-dimensional porous $Ti_3C_2T_x$-NiO composite electrodes with enhanced electrochemical performance for supercapacitors *Materials* **12** 1–11

[120] Hu M, Hu T, Li Z, Yang Y, Cheng R, Yang J, Cui C and Wang X 2018 Surface functional groups and interlayer water determine the electrochemical capacitance of $Ti_3C_2T_x$ MXene *ACS Nano* **12** 3578–86

[121] Karikalan N, Karuppiah C, Chen S-M, Velmurugan M and Gnanaprakasam P 2017 Three-dimensional fibrous network of $Na_{0.21}MnO_2$ for aqueous sodium-ion hybrid supercapacitors *Chem. Eur. J.* **23** 2379–86

[122] Zhong C, Deng Y, Hu W, Qiao J, Zhang L and Zhang J 2015 A review of electrolyte materials and compositions for electrochemical supercapacitors *Chem. Soc. Rev.* **44** 7484–539

[123] Lin Z, Rozier P, Duployer B, Taberna P-L, Anasori B, Gogotsi Y and Simon P 2016 Electrochemical and in-situ x-ray diffraction studies of $Ti_3C_2T_x$ MXene in ionic liquid electrolyte *Electrochem. Commun.* **72** 50–3

[124] Dall'Agnese Y, Rozier P, Taberna P L, Gogotsi Y and Simon P 2016 Capacitance of two-dimensional titanium carbide (MXene) and MXene/carbon nanotube composites in organic electrolytes *J. Power Sources* **306** 510–5
[125] Wang X *et al* 2019 Influences from solvents on charge storage in titanium carbide MXenes *Nat. Energy* **4** 241–8
[126] Jiang Q, Kurra N, Alhabeb M, Gogotsi Y and Alshareef H N 2018 All Pseudocapacitive MXene-RuO_2 asymmetric supercapacitors *Adv. Energy Mater.* **8** 1–10
[127] Wu W, Lin S, Chen T, Li L, Pan Y, Zhang M, Wu L, Gao H and Zhang X 2017 Performance evaluation of asymmetric supercapacitor based on $Ti_3C_2T_x$-paper *J. Alloys Compd.* **729** 1165–71
[128] Avireddy H *et al* 2019 Stable high-voltage aqueous pseudocapacitive energy storage device with slow self-discharge *Nano Energy* **64** 103961